MULTIYEAR AUTOMATED ANALYSIS OF AURORAL IMAGES TO CATEGORIZE IONOSPHERE IRREGULARITY LAYER

BY

DAVID STUART

Submitted in partial fulfillment of the
requirements for the degree of
Master of Science in Mechanical and Aerospace Engineering
in the Graduate College of the
Illinois Institute of Technology

Approved Seebany Datta-Barua
Digitally signed by Seebany Datta-Barua
DN: cn=Seebany Datta-Barua, o=Illinois Institute of Technology, ou, email=sdattaba@iit.edu, c=US
Date: 2020.04.27 08:34:34 -06'00'

Advisor

Chicago, Illinois
May 2020

ACKNOWLEDGMENT

My sincere gratitude goes to the members of both the SAGA team and the IIT Space Weather Lab, without whose support this work would not have been possible. Chiefly Dr. Datta-Barua guided this project and provided encouragement tirelessly through the last year-and-a-half that this work was active. Dr. Hampton's observations formed the impetus for a physically-driven, keogram, cloud detection method, and his knowledge of auroral spectra was equally integral. His repository of aurora images and maintenance of Poker Flat cameras was prerequisite for this work. I would also like to extend my thanks to Dr. Pervan for sitting on my committee and reviewing my thesis.

As this work relied on previous SAGA developments, this work would not have been possible without any of the current or prior members. The database of GPS scintillation events was created by Dr. Su and extended by Vaishnavi Sreenivash, who also created E/F designations via radar measurements.

My colleagues at the IIT Space Weather Lab were extremely generous sharing technical knowledge, especially Dr. Parvizi for his aid with computational tools, and Dr. Wang for insight on ionosphere behavior. My lab friends Shahrukh Khan, Li Pan, Heejin Kim, and Aurora Lopez helped make work fun and enjoyable.

I would also like to thank my parents Steven Stuart and Ellen Wilson, whose love and support allowed me to pursue graduate studies.

This work was supported by NSF Award AGS-1651465. Any opinions, findings, and conclusions or recommendations expressed in this material are those of the author(s) and do not necessarily reflect the views of the NSF.

TABLE OF CONTENTS

LIST OF TABLES

LIST OF FIGURES

LIST OF SYMBOLS

Symbol	Definition
λ	wavelength (in context of aurora emission frequency)
t	time
θ	keogram elevation viewing angle
S	sensor keogram
M	measured keogram
M^*	background keogram
C	calibrated keogram
Y	flat field corrected keogram
i, j	pixel coordinates of standard (nonkeogram) 2D image
m	image or snapshot average intensity
F_{ij}	2D flat field image
D_{ij}	2D dark field image
G_{ij}	2D flat field gain
C_{ij}	2D flat field corrected image
T_0, T_f	identified cloudy interval
$\bar{G}$	keogram flat field gain
$\bar{F}$	keogram flat field image
c_v	coefficient of variation
ν	noise
δ	angle between magnetic zenith and pixel direction
α	electron characteristic energy

ABSTRACT

This thesis presents a method of automated analysis of auroral all-sky images (ASIs) to determine the ionospheric layer of plasma irregularities. These irregularities can perturb radio signals in an effect called scintillation, degrading and at worst preventing signal reception. One key question about scintillation-causing irregularities is whether they occur in the E or F layer of the ionosphere, whose dynamics differ.

Previous studies have shown Global Positioning System (GPS) scintillation to be correlated with aurorae. The Scintillation Auroral GPS Array (SAGA) at Poker Flat Research Range, Alaska, was used to detect thousands of GPS L1 and L2C scintillation events over 2014-2015. Collocated auroral images of emissions are recorded nightly by both a keogram spectrograph (measuring intensity along a single longitude vs time) and an ASI filtered at 630.0 nm (red), 557.7 nm (green), and 427.8 nm (blue) wavelengths.

In this work scattering layers are hypothesized based on optical measurements, through automated filtering of keograms followed by spectral analysis of aurorae, which tend to occur with these irregularities. A cloud detection method using the North-South keogram is implemented, where a time-averaged, intensity-corrected characteristic snapshot of cloudy times was built as a baseline response, and used as the gain in a flat field correction-like step to normalize the cloudy sky appearance. The coefficient of variation c_v is used as the test statistic to determine cloudy times. Cloud-free ASIs have the location of scintillating PRNs identified, and the ratio of red oxygen 630 nm to blue nitrogen 428 nm emissions in that direction. With an auroral model of characteristic energy, ratios above 0.5 are categorized E-Layer and ratios below F-Layer.

Multiyear ASI irregularity layer determinations are used to categorize 364 of the initial 4174 SAGA scintillation events. A 77% majority of the events are

hypothesized to be F-Layer based on ASI spectral classification. This disagrees with prior PFISR categorizations, which found scintillation events to be majority E-layer. This presents an outstanding question as to the possible reasons for the difference.

CHAPTER 1
INTRODUCTION

The Earth's atmosphere transitions gradually from the familiar environment at ground level to become sparse and energetic as it meets the solar wind in outer space. It is broken into different regimes (sometimes overlapping) dominated by different effects. The ionosphere [1] is the region where electron density peaks, and plasma dynamics dominate. It extends from 50-2000 km, though definitions vary [1].

The ionosphere is ionized by solar UV radiation, as well as energetic particles carried by solar wind and cosmic radiation [1]. Neutral gases composing the atmosphere react forming ions and free electrons. Variations in solar activity change composition, electron density, and height of the ionosphere [2]. These free electrons have the potential to interact with passing electromagnetic (EM) waves, with implications for radio communications and other human activities.

Though dynamic, the ionosphere generally has layers [1], shown in Fig 1.1 produced by NOAA [3]. The lowest, D layer, appears daytime with solar radiation at 50-95 km [1]. Above it is the E-region between 90-150 km, containing a local maximum in electron density. Highest is the F-region from 150-2000 km, extending to the edge of space, and usually containing the peak ionospheric electron density.

Rather than the average profile the true ionosphere shows variation in height as well as spatial structuring. Structuring in electron density and accompanying electron density gradients are termed ionospheric irregularities. These produce interference with electromagnetic signals at specific frequencies [4]. Irregularities at high magnetic latitudes are often created by solar events (flares and coronal mass ejections) [1].

1.1 Scintillation

The electron density structures of irregularities cause refractive and diffractive

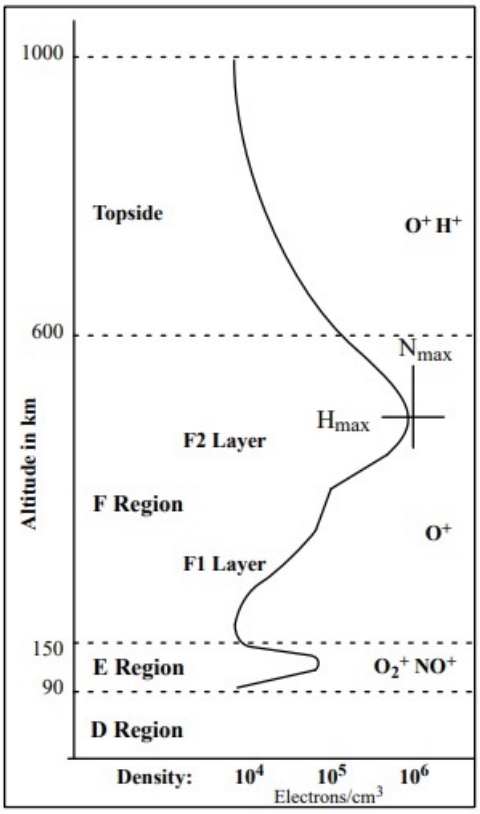

Figure 1.1. Profile of of ionosphere electron density, showing D-, E- and F-region, image courtesy NOAA [3]. Slightly different height definitions than given by Tascione [1].

interference of passing EM waves. Called scintillation, this can in general include rapid changes to both phase and amplitude of the signal. Figure 1.2 illustrates.

Scintillation often has been observed for the radio frequencies of Global Navigation Satellite Systems (GNSS) in the poleward auroral zones. This is an engineering challenge: at worst a loss-of-lock in GPS and other GNSS signals, but also smaller so less easily detected errors. In this way space weather presents a challenge to human activity. Conversely scintillation is a means of probing the ionosphere and expanding scientific knowledge by using existing infrastructure, without needing new, dedicated satellites.

For the L1 (1575.42 MHz) and L2C (1227.60 MHz) frequencies of GPS signals,

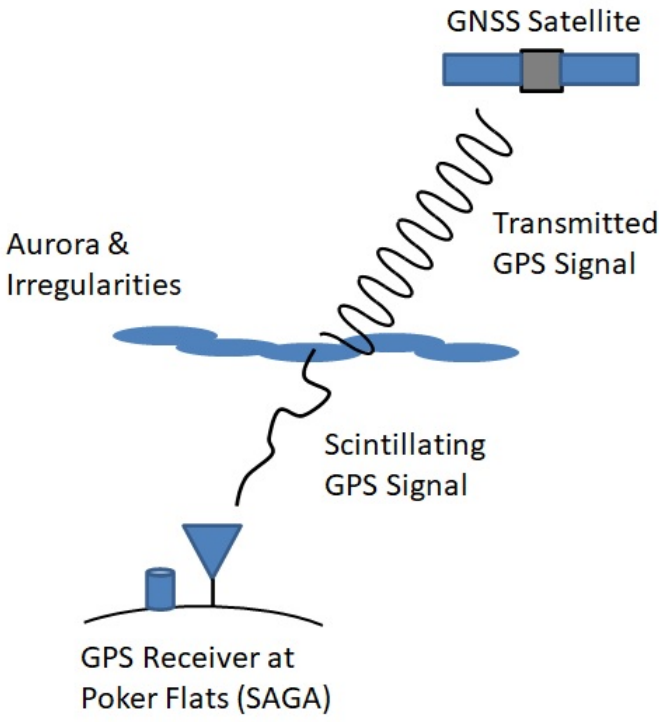

Figure 1.2. Scintillation of GNSS signal passing through ionospheric irregularities, detected by ground receiver.

scintillation is produced in the auroral zone by about 100 m scale irregularities [4]. Scintillation intensity is characterized by the S_4 amplitude scintillation index and σ_ϕ phase scintillation index [5]. These indices measure of the standard deviation in respectively signal power and phase, over about a minute time interval. Phase scintillation absent significant amplitude changes is the most common mode in the auroral zone [5]. Other remote sensing work using GNSS seeks to acquire the full signal [6], or maintain signal lock in the presence of scintillation.

Scintillations are an active area of study [5, 7, 8], in which one question is the difference in occurrence and effects of E- and F-layer irregularities. The E-region has neutral densities great enough to impact plasma dynamics through collisions, while the F-region has very sparse neutrals with a correspondingly lower rate of collisions [1]. Scattering height and layer informs the active mechanics, so layer categorizations

are of scientific interest. Methods in addition to prior work [5, 7] also serve to improve confidence.

1.2 Contributions

The objective of this thesis is to develop an automated process to categorize the ionosphere irregularity layer, whether E or F, from auroral images, both from a meridian spectrograph and all-sky camera. Contributions are overviewed in this section, and described in detail in Chapter 3 and Chapter 4.

Contribution 1 is an automated keogram cloud detection method based on visual observations of the signature of cloudy behavior in a keogram. From calibrated keograms in suitable regions, times of clean auroral light are found. I develop and apply a novel flat field correction, with an average flat field constructed from an interval of total cloud cover. The coefficient of variation of corrected snapshots is used as a metric for cloud cover, and cloud free intervals are determined.

Contribution 2 is spectral analysis of all-sky images (ASIs) to provide ionospheric layer categorization of irregularities. Cloud-free intervals, SAGA scintillation lists, and ASI timestamps are compared for overlap. Events with PRNs near magentic zenith are found, and an auroral chemistry model is applied to create thresholds for E- vs. F-region events. Categorizations are made for all suitable 2014-2015 events, and found to disagree with prior radar designations.

CHAPTER 2

BACKGROUND

This chapter reviews ionosphere and aurora mechanics to establish the relation between specific auroral emissions and the irregularity scattering layer. Past research which this work builds upon is also described.

2.1 High Latitude Ionosphere and Aurora

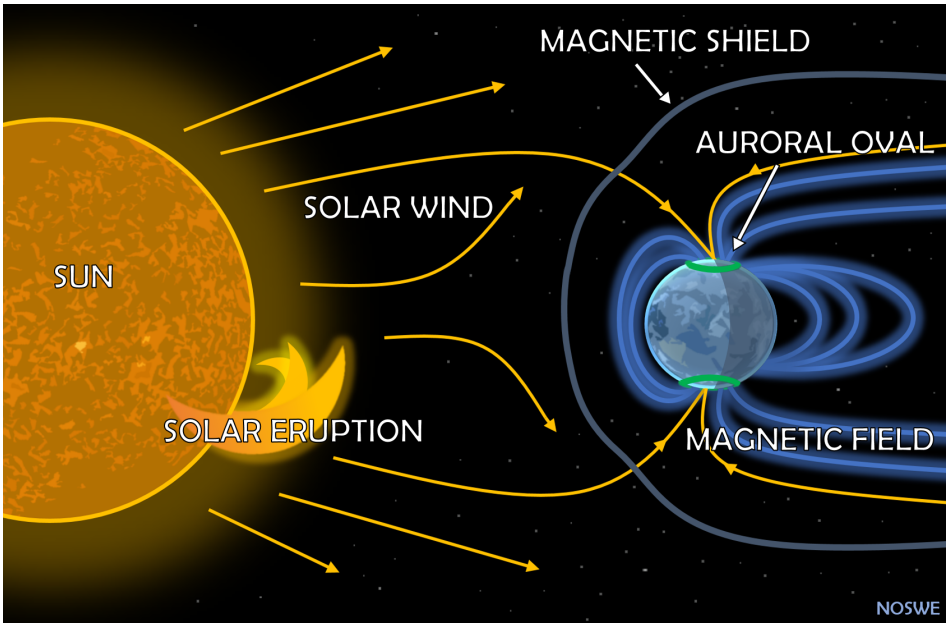

Figure 2.1. Solar wind entering Earth's ionosphere where Earth's magnetic field reconnects with solar wind magnetic field lines, creating the auroral zone near the poles, credit [9].

Like a boat at sea, the solar wind governs the Earth's space weather environment. Shown in Fig 2.1 from NOSWE [9], plasma from the sun flows outward, and is mostly deflected by the Earth's magnetosphere [1]. However in two regions of the magnetosphere, one sunward and one from the magnetotail, Earth's magnetic field lines reconnect with the magnetic field of solar wind, creating a conduit for particle precipitation. The intersection with the atmosphere forms a luminous auroral oval at both poles (green rings in Fig 2.1) from resulting ionization and chemical reactions.

Solar electromagnetic radiation, which is not deflected by the magnetosphere, also ionizes the upper atmosphere globally [1]. Together these effects create the Earth's ionosphere from 50-2000 km altitude, with variations for local time and solar activity [1].

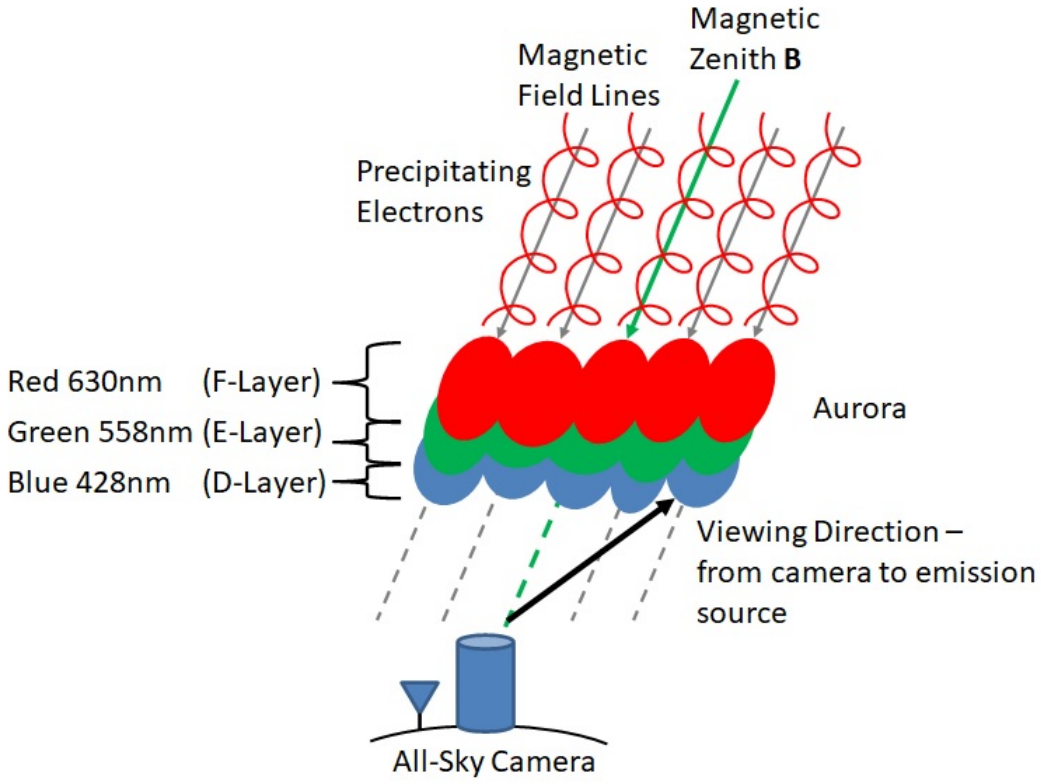

Figure 2.2. Electron precipitation leading to visible spectrum auroral emissions, and corresponding ionosphere layer. A ground camera only looks along field lines (which restrict electron motion) when viewing the sky in the direction of magnetic zenith.

In the auroral oval, electrons originating in solar wind ("primary electrons") spiral along Earth's magnetic field lines until they collide with the atmosphere, per Fig 2.2. Primary ionization, dissociation, and excitation feed into a connected system of auroral processes [2, 10], interacting with both ions and neutrals. Electron transport is restricted to gyration along magnetic field lines [1]. Transitions of excited species produce photons of specific energies (wavelengths) producing the emissions described

in this work [1, 2, 10].

Three emissions are of interest in this work. 630 nm (red) emits from atomic oxygen transitioning from lowest excited state $O(^1D)$ to ground, with the main source primary electron impact with ground atomic oxygen [2], and is predominately seen in the F-region. It has a radiative half-life of about 25 s [10], but is collisionally deactivated by molecular nitrogen below 180 km [2]. Green light at 558 nm emits from atomic oxygen transitioning from the $O(^1S)$ to the $O(^1D)$ state, driven by both primary impact, dissociative recombination, and energy transfer from excited molecular nitrogen, and is observed in the E-region [2]. Radiative for 1 s, it is collisionally deactivated by both atomic oxygen and molecular nitrogen [2]. Wavelength 428 nm (blue) emits from molecular nitrogen transitioning between excited states, and originates where nitrogen is more concentrated in the D- and E-Region [2].

Auroral emissions have long been the subject of study, with column-integrated models developed in by Rees and Luckey [2] and Strickland [10], among others. These consider the view of a ground observer seeing the sum of emissions from varying emission heights. These models describe total emissions to a ground observer based on given Maxwellian electron distributions with peaks at electron characteristic energy α. The reverse relation from observed emissions to α is then established. Fig 2.3 shows the Rees and Luckey model [2], relating the 428 nm intensity (x-axis), 630 nm/428 nm emission ratio (y-axis), and α (contour lines). Additionally, Banks [11] observed that $\alpha > 2$ keV leads to E-region aurora below 150 km, which is overlaid on Fig 2.3. Finally, relating back to scattering irregularities, prior works have observed aurorae accompanying scintillation [7, 8].

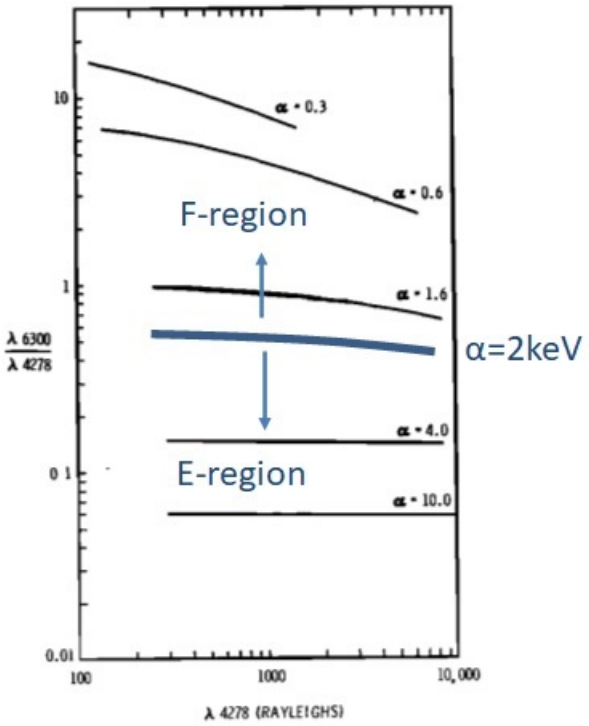

Figure 2.3. Relation between 428 nm (blue) aurora intensity, 630 nm/428 nm ratio (red/blue), and electron characteristic energy α, credit [2]. Blue annotations shows E/F transition α described by [11].

2.2 Instruments and Prior Work

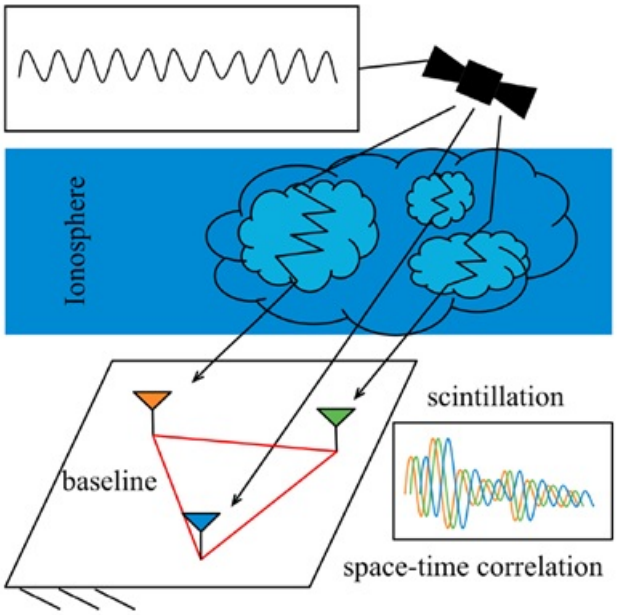

Figure 2.4. Spatial variation of ionosphere irregularities leading to time delays in GNSS scintillations measured by SAGA spaced-receiver array, credit [5].

Prior work has measured GPS L1 and L2C scintillation over 2014-2015 using the Scintillation Auroral GPS Array (SAGA) in the auroral zone at Poker Flat, Alaska [5, 7]. Composed of multiple physical receivers with baseline separations on a scale of 100 m to 1 km, low-rate 0.01 Hz scintillation indices and high-rate 100 Hz signal amplitude and phase data have been measured, and are publicly accessible [12]. The spatial configuration of the array (Fig. 2.4) allows observation of irregularity motion by comparing the high-rate 100 Hz power and phase data from each receiver. Intervals of strong scintillation in amplitude or phase have been assembled in a scintillation event list for 2014-2015 [7]. GNSS signals have found other fortuitous uses in remote sensing; for example other researchers have used reflected GPS signals to evaluate ice cover on water [13].

Collocated with the GPS receiver is the Poker Flat Incoherent Scatter Radar

(PFISR). Operating at about 450 MHz, PFISR measures electron densities, electron drift speeds, and electron temperature [7]. Radar data is publicly accessible [14]. By combining measurements from two radar beam modes suitable for different altitudes, peak electron densities during scintillation events have been used to categorize the corresponding scattering layer of the ionosphere [7].

Also sited at Poker Flat are a keogram spectrograph and all-sky camera (ASC) operated by Prof. Don Hampton [15]. 2014-2015 keogram spectrograph data has been stored for six emission wavelengths: the three already described as well as three other auroral emissions (486.0 nm, 520.0 nm, 670 nm) not used in this work. Additionally, a background keogram is taken at each of the six wavelengths, whose details are given in Chapter 3. Keogram spectrograph data is also publicly available [15]. Unlike a 2D image, the keogram shows a timeseries of 1D column snapshots (13s cadence). As shown in Fig. 2.5, meridional slices of the sky from the southern-to-northern horizon create columns (viewing angle θ is the y-axis). Snapshots of the sky through the night are stacked horizontally, so the x-axis shows time t from dusk until dawn, i.e., the keogram can be thought of as a video of a single slice of the night sky. Auroral arcs tend to be aligned East-to-West across the sky [1], so perpendicular snapshots capture them.

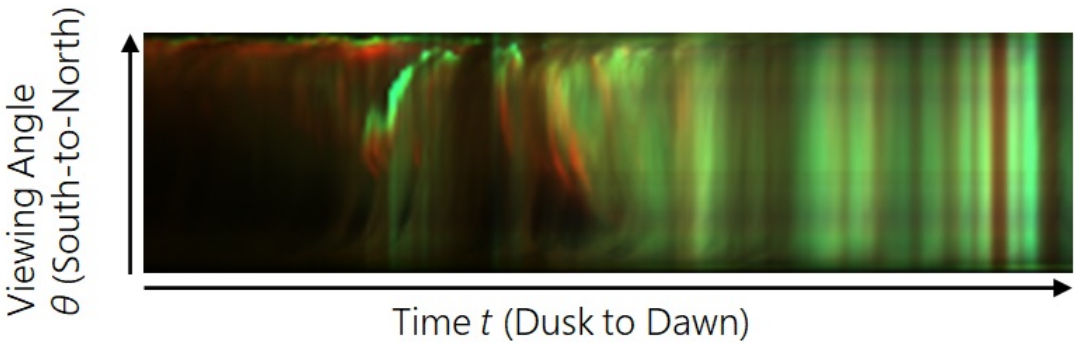

Figure 2.5. Summary red, green, blue (RGB) keogram for January 1, 2014, credit [15].

The ASC is a white-light camera with physical filters for the three auroral emissions - 428 nm (blue), 558 nm (green), and 630 nm (red). All-sky images (ASIs) are taken in red-green-blue succession over 12.5 s. The ASC operates from dusk through dawn, and images are available online [15].

2.3 Background on digital image correction

In charge-coupled device (CCD) cameras at native resolution, a pixel corresponds to a (small) physical sensor in the total sensor array. Manufacturing variations yield non-uniform pixel response, both per-pixel and on a row/column basis. "Vignette" is an intensity distortion created by the lens edges, where scene light strikes the sensor array at an incident angle instead of head on, causing lower apparent light at the edges of the image [16].

Flat field correction removes constant-in-time aberrations due to both sensor variation and vignette [16]. Flat field correction is a technique used to treat for lens and sensor effects [17], to create a corrected image (see Fig. 2.6a). It models each pixel, with pixel indices i, j, having a unique bias (response to zero light) and linear response to input. The uncorrected image R_{ij} is adjusted to arrive at the corrected radiance of the subject C_{ij}. Two reference images are used: the first called the dark field image D_{ij} is taken with the lens blocked to measure the sensor bias (see Fig. 2.6b). The second reference is the flat field image F_{ij}, taken of uniform light, to measure individual pixels' responses to the same (nonzero) input.

The brightness of the uniform light m used to create the flat field is found by subtracting the dark field from the flat field at every pixel, then finding the average pixel value as given in Eq. 2.1. The dimensionless flat field gain G_{ij} is constructed by dividing m by the difference of the flat field and the dark field per Eq. 2.2 (see Fig. 2.6c). The reciprocal of G_{ij} can be thought of as the dimensionless flat field. Finally,

the uncorrected image R has the dark field D subtracted, and is multiplied with the gain to arrive at the final corrected image (Eq 2.3 and Fig. 2.6d).

$$m = \frac{\Sigma_{i=1}^{M}\Sigma_{j=1}^{N}(F_{ij} - D_{ij})}{MN} \tag{2.1}$$

$$G_{ij} = \frac{m}{F_{ij} - D_{ij}} \tag{2.2}$$

$$C_{ij} = G_{ij}(R_{ij} - D_{ij}) \tag{2.3}$$

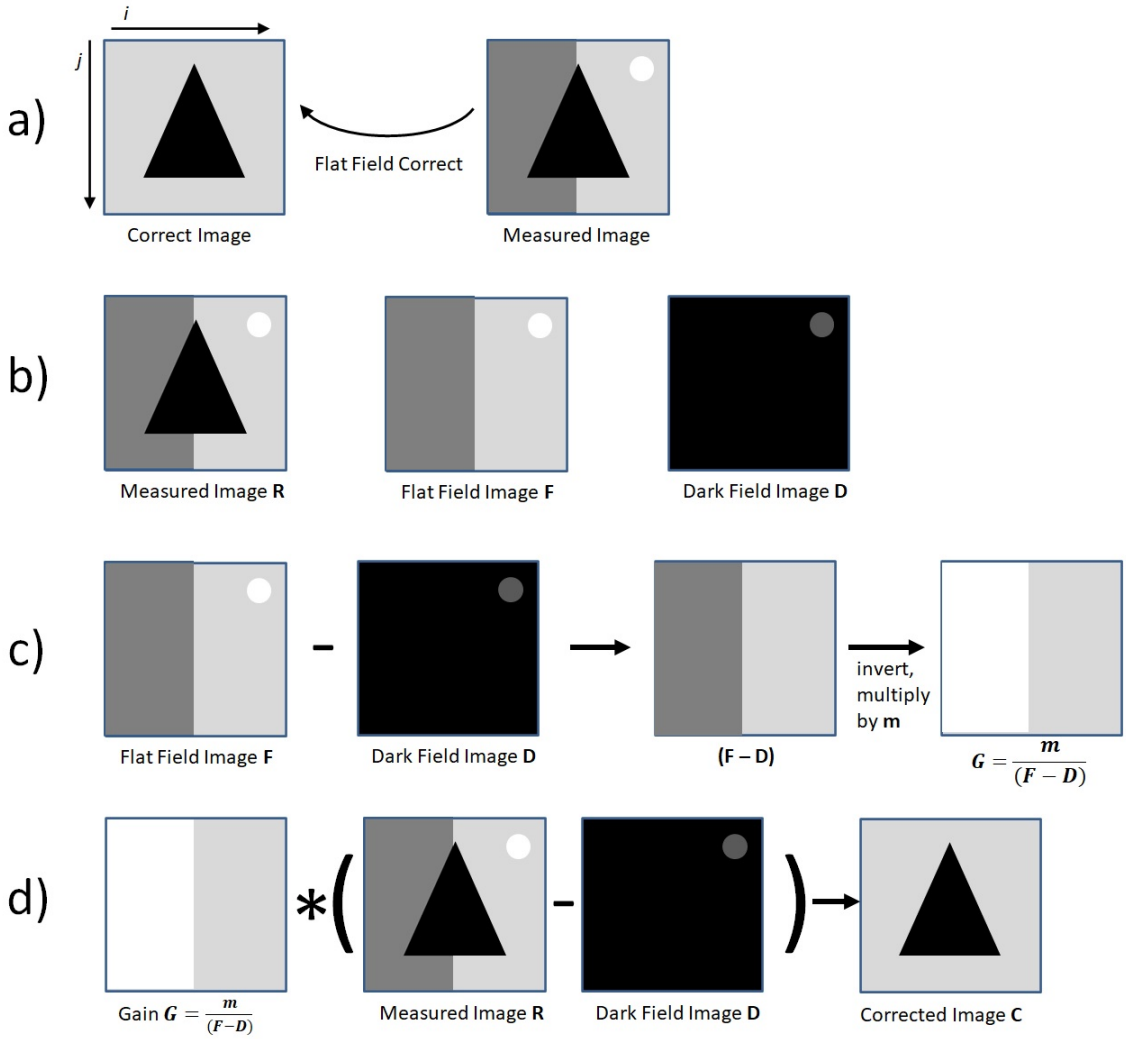

Figure 2.6. 2D flat field correction steps. (a) Desired corrected image and measured image. (b) Images taken by camera: measured image R, reference flat field image F and dark field image D. (c) Steps for construction of flat field gain G. (d) Correction of image R with gain G and dark field D to find corrected image C.

CHAPTER 3
CLOUD DETECTION FROM KEOGRAMS

Night sky camera images must be cloud-free for analysis of aurorae. Keograms recorded by a separate instrument, a meridian spectrograph [15], are used to determine cloud-free intervals. This chapter describes that method: automated identification of times with negligible sunlight, keogram calibration, and cloud detection from calibrated keograms. The result is time intervals estimated to be cloud-free, without the need to examine all-sky images. Figure 3.1 summarizes the processing that will be described in detail in this chapter. Section 3.2 discusses the first five blocks of the processing. Section 3.3 covers the adaptation of flat-field correction being introduced in this work, and Section 3.4 defines the coefficient of variation and demonstrates its use as a test statistic for cloud detection.

3.1 Keogram Advantages Over All-Sky Image

Keograms offer the advantage of using significantly less storage than full images of the night sky (or a timeseries of them as a video). For two years of recording, all keogram data was 6.0 GB, while all camera data was 2.8 TB (when both use uncompressed formats). Hosted by the Geophysical Institute in Fairbanks, Alaska [15], transfer of full camera data would require mailing hard drives. The portability of keograms allows some preliminary analysis and selection of image subsets for further analysis. Cloud detection directly from all-sky image has been investigated by other researchers, including using neural network trained with labeled images [18], and feature extraction to detect cloud or auroral signatures [19]. However these techniques are not physically driven, and as black box methods, don't necessarily lead to insight.

From previous work in auroral imaging, researchers have qualitatively observed keograms to be smeared during cloudy periods [20]. Specifically, when cloudy, the

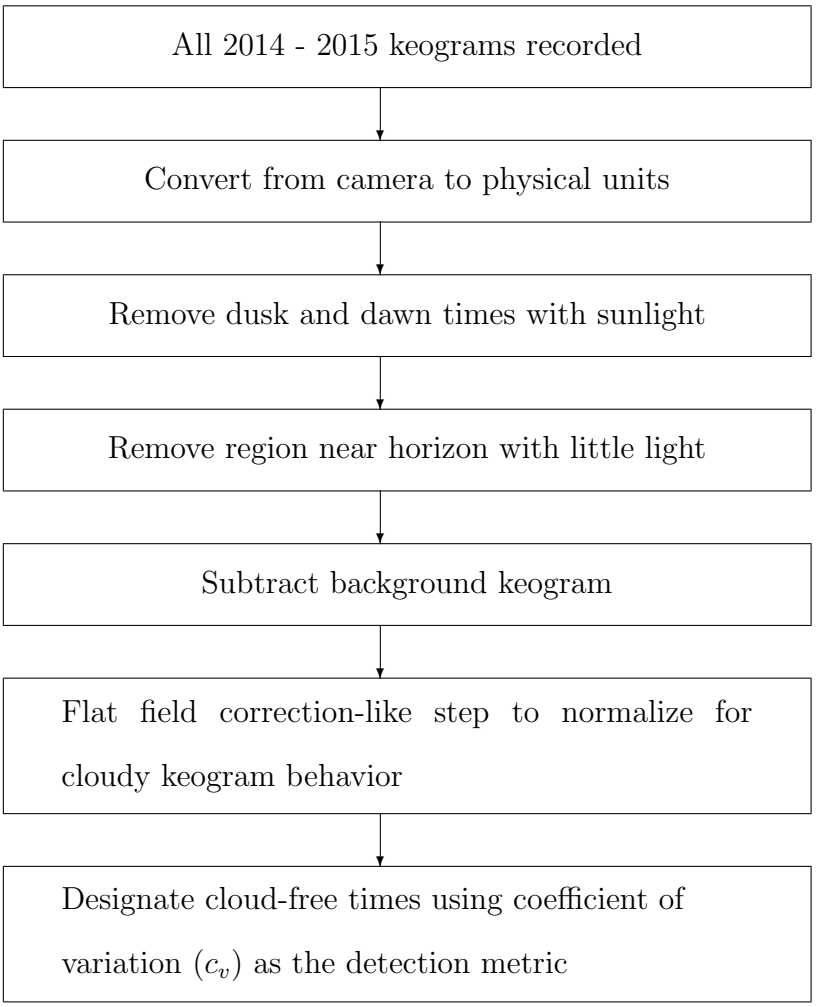

Figure 3.1. Overview of keogram processing and cloud detection

keogram looks something like a "barcode," in which the night sky is uniform with viewing angle (the keogram's vertical axis), but can change with time (horizontal axis). An example is shown in Figure 3.2, where a barcode overlay [21] demonstrates behavior seen in the later night. Intuitively, one can imagine a very cloudy sky lit from above by aurora, so auroral light appears smudged or spread out across the sky. The cloud detection method described in subsequent sections is an attempt to formalize the detection of the time intervals that appear as "barcodes," i.e., cloudy.

Figure 3.2. Summary RGB keogram for January 1, 2014 [15], modified with a consumer product barcode (from [21]) overlaid to emphasize cloudy appearance during later half of night. The green, red, and black vertical stripes in the right part of the plot in which a cloudy night sky is scattering auroral light uniformly at all viewing angles, mimic the appearance of a consumer product "barcode."

3.2 Trimming and Calibrating Keogram Data

Certain portions of keogram data are not suitable for cloud detection. Though the keogram spectrograph records the entire sky from dusk to dawn, auroral light is best captured in the middle of the night, and away from the horizon. Sunlight overwhelms auroral light for a time after sunset, and for a time before sunrise. Near both north and south horizons, the keogram records dimmer and inconsistent light.

Using already measured camera calibrations for 13s spectrograph exposures k_λ [20] shown in Table 3.1, the raw sensor data S_λ at a given wavelength λ is converted from camera units to photon flux M_λ in Rayleighs per Eq. 3.1.

$$M_\lambda(t,\theta) = k_\lambda S_\lambda(t,\theta) \tag{3.1}$$

where S_λ is the spectrograph's direct sensor measurement in units of camera counts at time t and elevation angle θ measured from 0° north to 180° south, k_λ is each of the 3 wavelength-specific calibration factors, and M_λ is the keogram in Rayleighs.

Table 3.1. Keogram Spectrograph Calibration from Sensor Counts to Rayleighs

Wavelength λ (nm)	Spectrograph Calibration for 13s Exposure k_λ (Rayleighs/count)
427.8	25.4
557.7	6.2
630.0	7.8

Figure 3.3 shows the unprocessed greenline (558 nm) measured keogram M_λ for the entire night of January 1, 2014. Times close to dusk and dawn, when the record starts and ends, are so bright the instrument saturates at over 10^5 Rayleighs. Relative to sunlight, aurora is orders of magnitude fainter. Looking at all-sky camera images at the start of the record, Fig. 3.4 shows sunlight on the southern horizon. The sunlight in these images makes them unsuitable for active ionosphere categorization

(Chapter 4). After 02:30 UT the sunlight disappears, then reappears preceding dawn, which is briefly seen before the keogram record ends (light on right edge of Fig 3.3, which appears faint since the colorbar is scaled to the keogram saturation value).

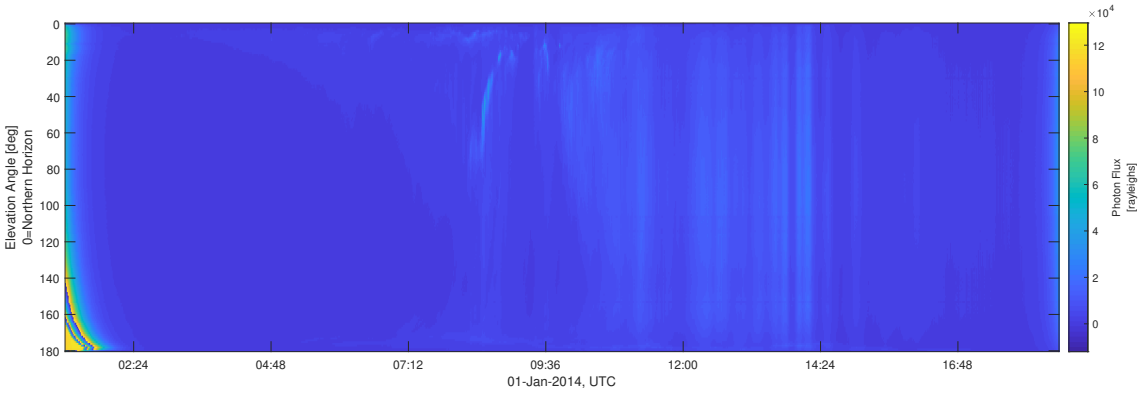

Figure 3.3. Measured keogram M_λ for 558 nm (green) wavelength on January 1, 2014, in Rayleighs.

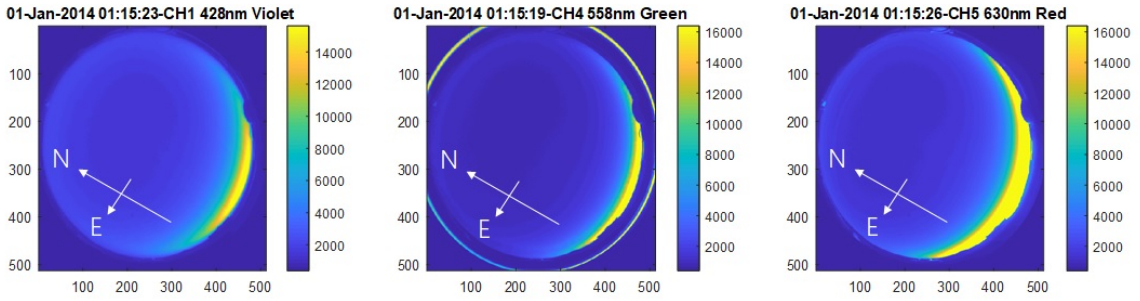

Figure 3.4. False color all-sky camera images in Rayleighs at the keogram initial recording time on January 1, 2014, showing scattered sunlight post-sunset. (left) 428 nm, (center) 558 nm, (right) 630 nm.

Scattered sunlight intensity during sundown is a function of the sun's angle below the horizon. Images across a range of seasons, both midwinter and spring nights were considered (since Poker Flat is near the Arctic Circle, night nearly disappears in summer). To crop the keogram in time to remove saturation, a sun elevation angle cutoff of 12° below horizon (102° from zenith) was found acceptable, balancing the need to have sunlight-free images with retaining as much data as possible. This threshold for January 1, 2014, is shown in Fig. 3.5 post-sunset. Weak sunlight on

the order of faint aurora is present near the horizon, but not higher in the sky where spectral analysis occurs. Note the range of the color axes is reduced nearly two orders of magnitude from Figure 3.4 to Figure 3.5.

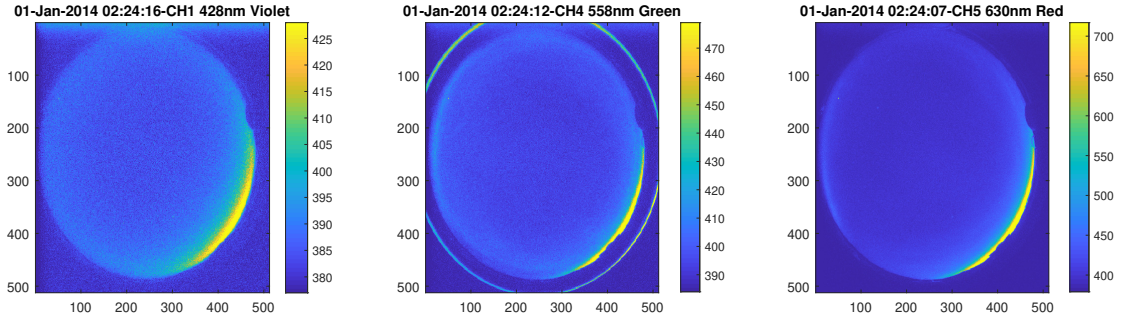

Figure 3.5. False color all-sky camera images in Rayleighs at beginning of suitable darkness, computed using sun dip angle.

The horizon region of the keogram tends to show less intense and inconsistent light. Referring back to the keogram in Fig 3.3, the horizons (top and bottom edge) appear almost jagged in the region from inconsistent light. Sunlight also appears here first. The region 10° from both horizons is discarded, leaving a keogram spanning $\theta = [10°, 170°]$.

After cropping the keogram, measurement error sources must be removed. A model of the photon flux measurement M_λ is shown in Eq. 3.2, with the dependent variables t and θ dropped for brevity. For understanding this model, some explanation of underlying physics and sensor model is helpful. The measured keogram spectograph M_λ is narrowly filtering at the 3 wavelengths of interest: 630.0 nm, 557.7 nm, and 427.8 nm. The sources of light at wavelength λ are as follows. Physically present sources, along the ray-path in the look-direction from each spectrograph pixel, consist of auroral light a_λ (narrow emissions of specific chemical reactions), but also undesired broadband emissions b_λ from light pollution. Clouds if present add a scattering effect c_λ, so the camera sees indirect light (i.e. $c_\lambda = 0$ during cloud free times). Keogram sensor bias is modelled as a constant offset β_λ and a general noise term ν_λ encapsulates

both sensor noise and spurious emissions.

$$M_\lambda = a_\lambda + b_\lambda + c_\lambda + \beta_\lambda + \nu_\lambda \tag{3.2}$$

To remove error sources b and β, the next step is the subtraction of the background keogram from the measured keogram. The keogram spectrograph makes a second measurement M^*_λ by filtering at a nearby wavelength, whose components are shown in Eq 3.3. Broadband emissions b_λ are still present at the same strength, but the narrow auroral emissions a_λ drop. Cloud effects now apply only to the broadband emissions, represented by c^*_λ. The same sensor bias is seen, and noise remains.

$$M^*_\lambda = b_\lambda + c^*_\lambda + \beta_\lambda + \nu^*_\lambda \tag{3.3}$$

The background keogram M^* is then subtracted from the measured keogram, giving the calibrated keogram C_λ in Eq. 3.4. Broadband light b is thus removed. So is the common bias β, an important detail considering flat fielding during cloud detection. What remains is only direct auroral light a, differential cloud scattering $(c_\lambda - c^*_\lambda)$, and noise.

$$C_\lambda = M_\lambda - M^*_\lambda = a_\lambda + c_\lambda - c^*_\lambda + \nu_\lambda - \nu^*_\lambda \tag{3.4}$$

The calibrated keogram C_λ for 558 nm for January 1, 2014, is presented below in Fig. 3.6. The characteristic "barcode" behavior during cloud cover is more apparent. These remaining keogram portions have less spurious data, and are fed into the cloud detection as described below.

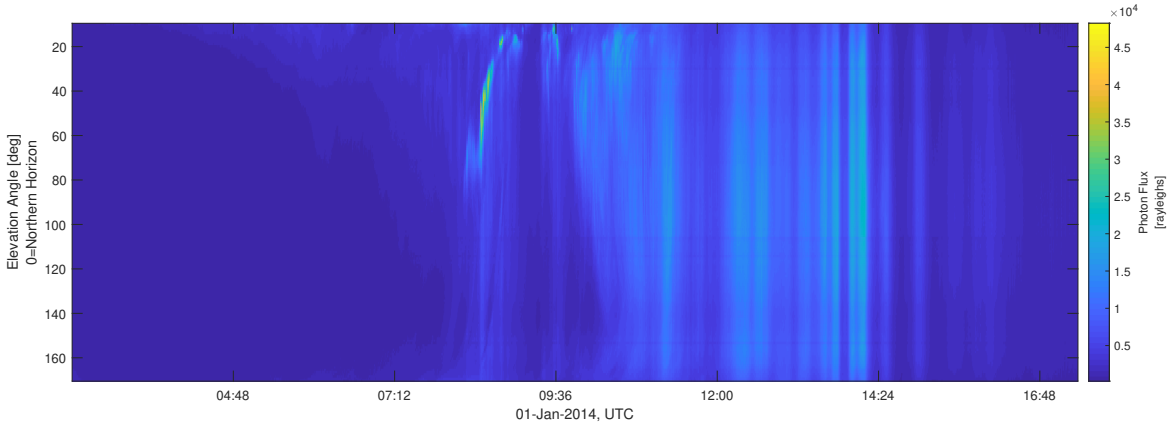

Figure 3.6. Trimmed and calibrated keogram C_λ for 558 nm (green) wavelength for January 1, 2014.

3.3 Flat Field Correction and Cloud Detection

This section describes the method used to detect cloudy periods, using the keograms C_λ calibrated per the previous section. The cloud detection combines three steps:

1. A novel flat field correction that tendency of a cloudy sky to scatter light uniformly with viewing angle.
2. Calculation of the coefficient of variation c_v at each keogram snapshot (keogram column).
3. A threshold to designate cloud-free or cloudy instants.

A novel flat field correction is applied to the keogram to further flatten the profile observed during cloudy times. Referring back to Figure 3.6, during the full cloud cover interval of the night e.g., from about 12:00 UT onwards, the observed "barcode" lines actually have some variation with elevation angle. Keogram snapshots during cloudy times have a vignette, in which light is less intense at low elevations (even after trimming the lowest 10°). Also seen are thin horizontal lines, and less distinct intensity peaks centered at about 30° and 150°, due to variations in the throughput of the optical train of the spectrograph. This backlit "cloudy profile" is consistent, though it brighten or dims as the illuminating light varies. The coefficient of variation metric, described later in this section, relies on the the cloudy snapshots being as uniform as possible, to provide a contrast with nonuniform auroral features, such as those at about 08:20 UT in Fig. 3.6.

Unlike standard 2D flat fielding described in the Background chapter, the keogram is a timeseries of multiple 1D snapshots. Each keogram snapshot (i.e., 1D column) is treated as an individual image. A true flat field must be constructed

without a reference image. For the keogram flat field, a snapshot of truly uniform light was not available (and one obtained at present would be not be meaningful for 5-year-old data, as the sensor properties may have changed), so in this work, properties of the cloudy sky are leveraged to create an average one.

For the flat field correction technique, first a descriptive overview is given with accompanying diagrams in Fig. 3.7, then more formal equations. The all-sky camera shows the cloudy sky as substantially uniform during complete cloud cover. Long time-averaging smooths out passing variations in the cloudy sky. During January 1, 2014, from 11:45:29-16:16:49 UT, 1501 keogram snapshots were identified in Fig. 3.7a as a continuous period of illuminated cloud cover.

First, each snapshot (i.e., 1D column) is normalized by dividing by its mean photon flux over θ (Fig. 3.7b). Combining the time series, the average flat field is found by time-averaging the normalized intensity at each viewing angle θ. The average flat field gain is simply the reciprocal of this (Fig. 3.7c). Snapshots of the uncorrected keogram C are multiplied by this gain, giving the flat field corrected keogram Y.

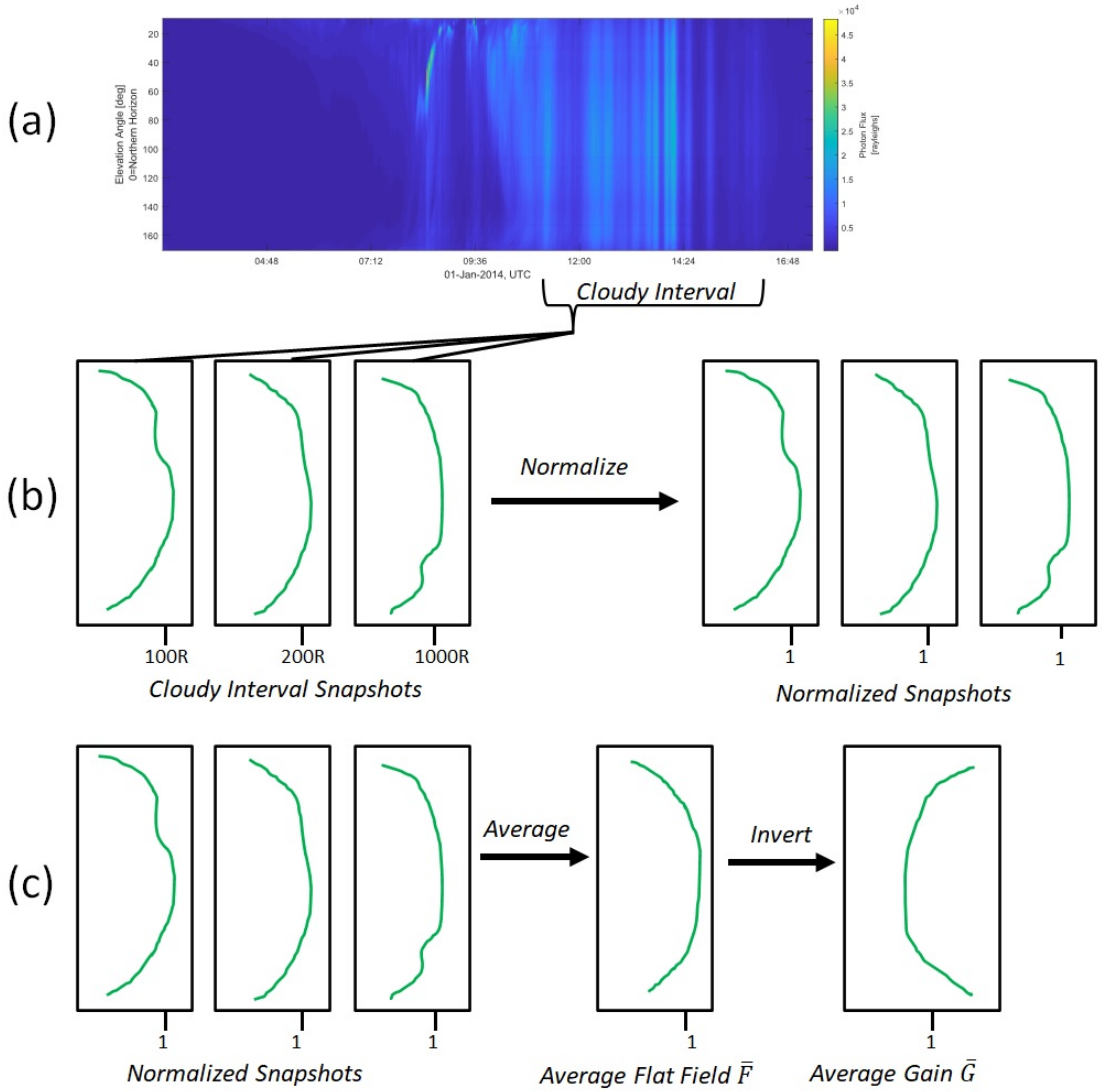

Figure 3.7. Cartoon demonstrating construction of average flat field gain from keogram data. (a) calibrated but not flat-field-corrected keogram C_λ of January 1, 2014, with location of cloudy interval. (b) shows normalizing of cloudy snapshots. (c) shows time-averaging of normalized snapshots to form average flat field gain $\bar{F}(\theta)$, and its reciprocal, the average flat field gain $\bar{G}(\theta)$.

The equations for keogram flat fielding are now presented as analogs to the 2D flat fielding. In the 2D form from Eqs. 2.1-2.3 a dark field term D representing camera bias is present. The keogram bias β was already removed when subtracting the background keogram (Eq. 3.4), so is dropped. The 2D uncorrected image term R_{ij} is replaced with the uncorrected keogram snapshots $C_\lambda(t, \theta)$. Two-dimensional pixel indices i and j are reduced to 1D index j, identifying a pixel look direction in a keogram snapshot. Time t now identifies different keogram snapshots indexed by i, where the period of verified cloud cover is from T_0 to T_f (January 1, 2014 11:45:29-16:16:49 UTC). Calculating the snapshot-average intensity m_λ is thus an average of every pixel θ_j within a given snapshot per Eq. 3.5, and is a timeseries unlike the single average found in Eq 2.1.

$$m_\lambda(t_i) = \frac{\sum_{j=1}^{N_\theta} C_\lambda(t_i, \theta_j)}{N_\theta} \tag{3.5}$$

The keogram flat field gain is first computed for cloudy snapshots as separate flat field images (i.e. a series of gains), then averaged together for an average gain $\bar{G}$. The individual snapshots' gains is shown in Eq 3.6, identical to the 2D method (Eq. 2.2) but excluding the D term since the calibrated C has already removed the bias.

$$G_\lambda(t_i, \theta_j) = \frac{m_\lambda(t_i)}{C_\lambda(t_i, \theta_j)} \tag{3.6}$$

The average gain $\bar{G}$ of these is found in Eq. 3.7. The timeseries of gain G is averaged at each pixel, by summing over time and dividing by the number of snapshots N_t present in the cloudy interval.

$$\bar{G}_\lambda(\theta_j) = \frac{1}{N_t} \sum_{i=1}^{N_t} G_\lambda(t_i, \theta_j) \tag{3.7}$$

The equivalent single cloudy snapshot that would give the the same flat field gain $\bar{G}$ is of interest for understanding what the profile of a cloudy snapshot tends

to look like. Working backwards and comparing the 2D gain equation Eq 2.2, if the average intensity is set to unity ($m = 1$), the average flat field $\bar{F}$ is simply the reciprocal of the gain $\bar{G}$, per Eq 3.8.

$$\bar{F}_\lambda(\theta_j) = \frac{1}{\bar{G}_\lambda(\theta_j)} \tag{3.8}$$

Finally the average flat field gain $\bar{G}$ is multiplied with all snapshots of the uncorrected keogram C, giving the corrected keogram Y in Eq 3.9

$$Y_\lambda(t_i, \theta_j) = C_\lambda(t_i, \theta_j) * \bar{G}_\lambda(\theta_j) \tag{3.9}$$

where the $*$ operator refers to element-wise multiplication along the θ dimension.

For the actual keogram data, Fig. 3.8 shows the flat field $\bar{F}$ calculated from the cloudy period during January 1, 2014. The left plot shows $\bar{F}_\lambda$ for $\lambda = 558$ nm, and the right plot shows $\bar{F}_\lambda$ for $\lambda = 630$ nm data. (Up to this point only 558 nm data had been shown previously.) For the greenline, maximum brightness near zenith and dimness near the horizons becomes apparent. Surprisingly, two symmetrical brightness peaks around 30° and 150° are also seen. What appeared as horizontal lines in the later period of January 1, 2014 keogram (Fig. 3.6), are shown clearly as individual pixels unusual to their neighbors, e.g., at 107° and 115°. The redline flat field shows asymmetry about zenith, with the peak at 70°, and the northern horizon brighter than the southern horizon. Otherwise the redline shows the same features as the greenline (i.e., two smaller bulges and aberrant single pixels).

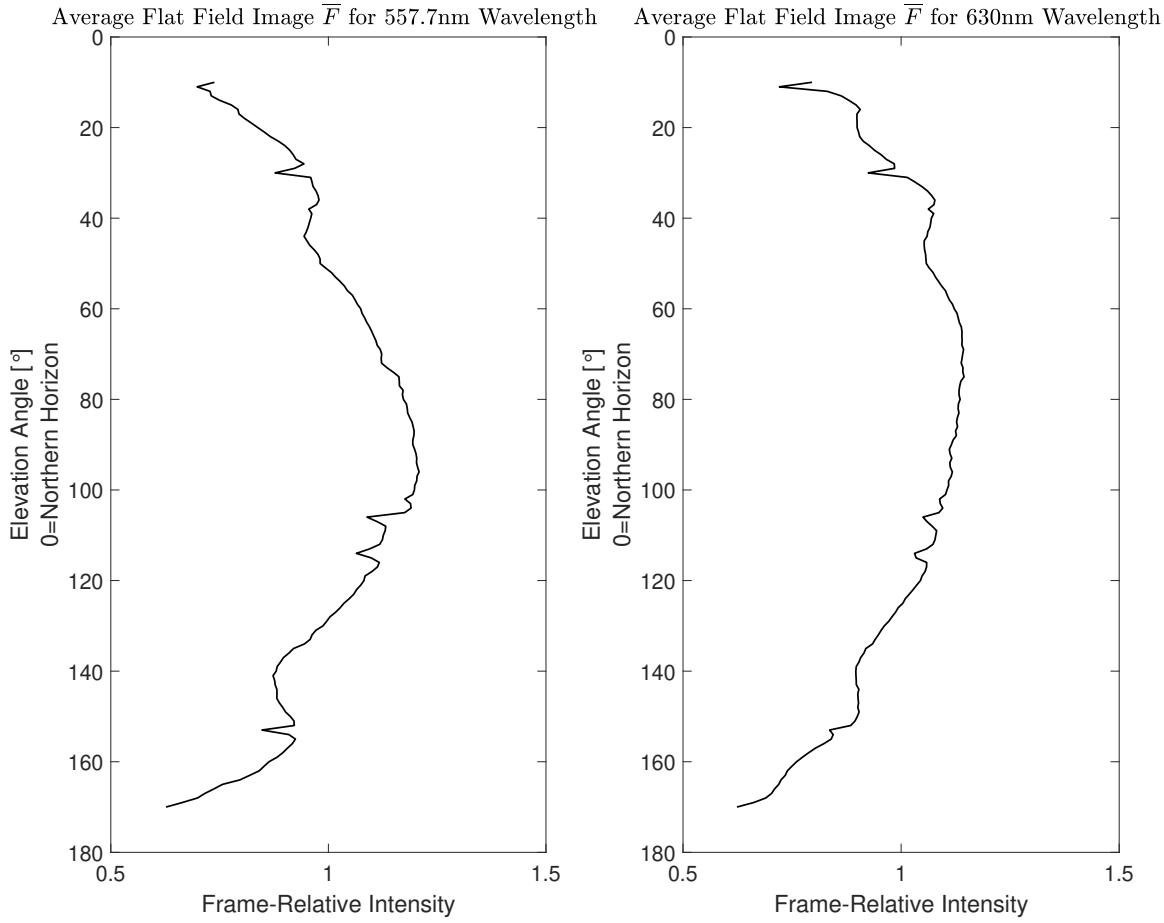

Figure 3.8. Flat field $\bar{F}$ for 558 nm (greenline) and 630 nm (redline) from cloudy period January 1, 2014.

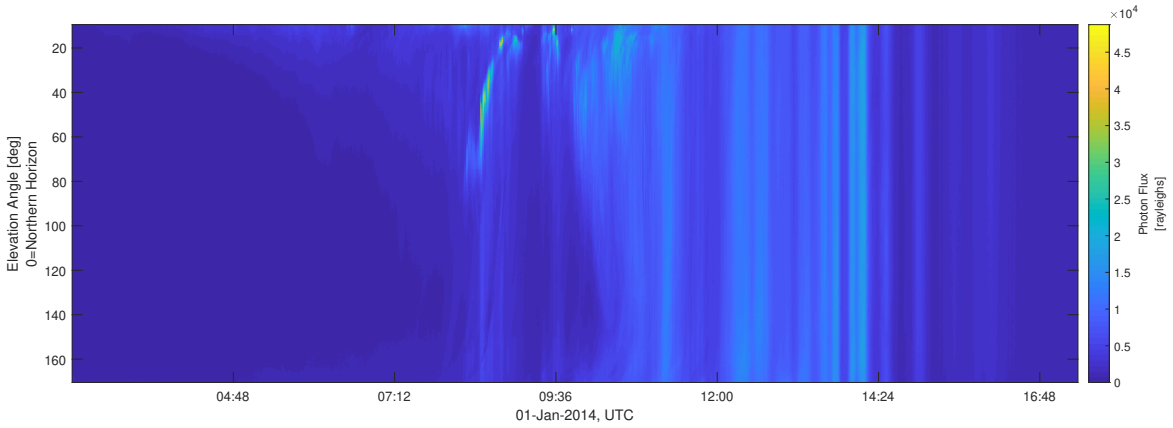

Figure 3.9. Flat field corrected keogram Y of January 1, 2014, 558 nm (green).

This flat field correction is applied to all keogram snapshots in the two-year set. The flat field corrected keogram $Y_\lambda, \lambda = 558$ nm for January 1, 2014, is shown in Fig. 3.9.

3.4 Test Statistic: Coefficient of Variation

As a cloud detection metric, the coefficient of variation c_v is calculated from the corrected keograms Y. In general, the coefficient of variation is the standard deviation σ of a set divided by its mean μ, per Eq. 3.10. It can be thought of as dimensionless standard deviation, in which standard deviation is normalized by the mean. Relating back to the "barcode" behavior, c_v serves as a test for uniform light across viewing angle θ. Standard deviation captures variations (greater for distinct auroral features), and mean μ accounts for the entire sky brightening or dimming (which creates brighter or dimmer "barcode" stripes effect within cloudy times). The average cloudy sky post-flat fielding would have a standard deviation near zero ($\sigma \approx 0$), while distinct auroral features during cloud free times lead to a higher value.

$$c_v = \frac{\sigma}{\mu} \tag{3.10}$$

The mean μ for each snapshot is simply the average over all viewing angles at a single instant, denoted by $y_\lambda(t_i)$.

$$y_\lambda(t_i) = \frac{\sum_{j=1}^{N_\theta} Y_\lambda(t_i, \theta_j)}{N_\theta} \tag{3.11}$$

The standard deviation is found similarly, arriving with the equation for coefficient of variation c_v at individual snapshots of Y at time t_i.

$$c_{v\lambda}(t_i) = \frac{\sqrt{\frac{1}{N-1}\sum_{j=1}^{N_\theta}[Y_\lambda(t_i, \theta_j) - y_\lambda(t_i)]^2}}{y_\lambda(t_i)} \tag{3.12}$$

The coefficient of variation is found this way for the entire two year set. Figure 3.10 shows the flat-fielded keogram $Y_\lambda, \lambda = 558$ nm for January 1, 2014, along with the coefficient of variation at each timestep in the lower plot. During the cloudy part of the night after about 12:00 UTC, the post-flat field c_v (red line) has significantly lower value than the pre-flat field c_v (black line), which is expected as the keogram Y is normalized to the cloudy appearance. In contrast, before 04:00 UTC the pre-flat field c_v is lower, as the flat field amplifies the faint light in the northern horizon.

Fig 3.10 underscores the importance of using c_v as a cloud detection metric *after* flat field correction. The c_v pre-flat field is found insufficient, due to the higher floor during cloudy times. This motivated the development of the keogram flat field method.

Thresholds for coefficient of variation c_v are chosen to designate cloud free vs. cloudy times. By observing true cloud cover seen by the all-sky camera over the nights January 1-5, 2014, and March 16-18, 2015, and comparing that with the behavior of the metric, thresholds were found. These are shown below in Eq. 3.13, where the 428 nm is ignored, and a lower cutoff is placed on the green c_v (0.25) than the red c_v (0.4). The green line shows generally clear behavior, while the red c_v shows wider swings, so a higher threshold is set for red. The blue keogram showed too much

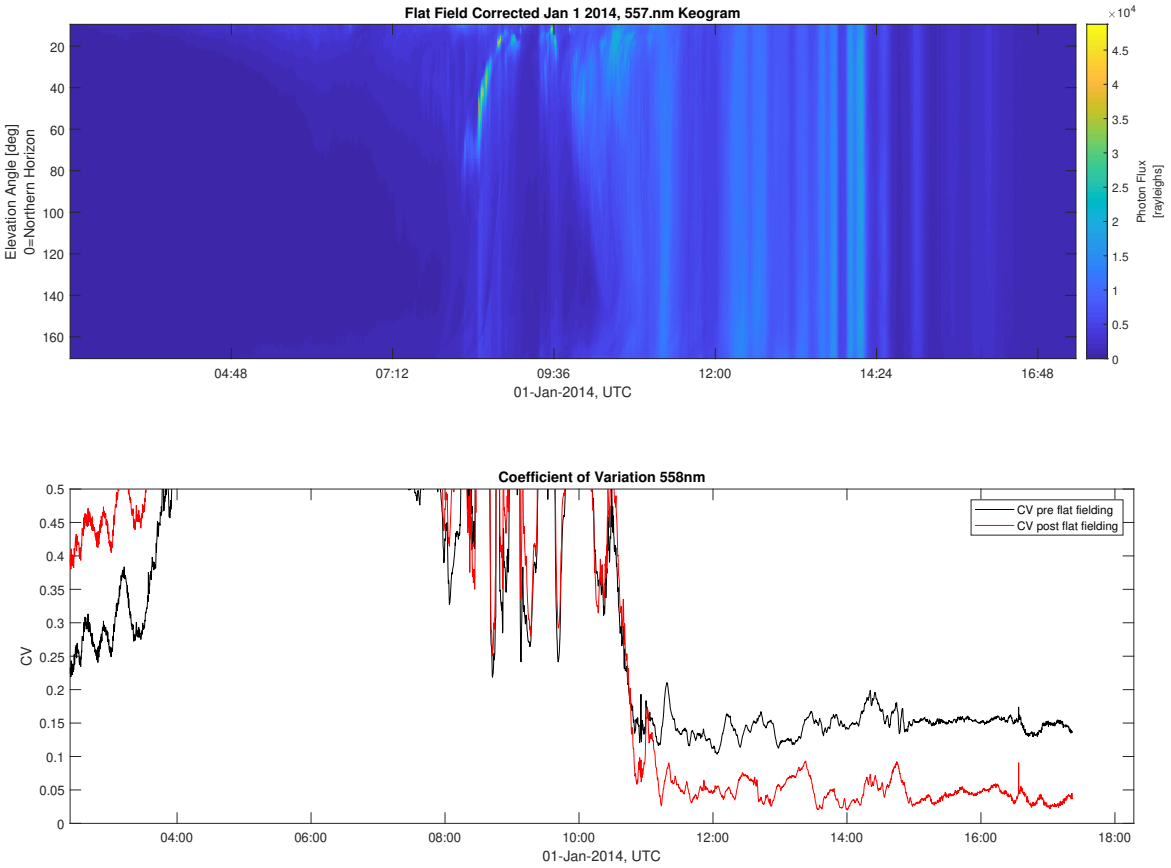

Figure 3.10. Flat field corrected keogram Y upper, and below the coefficient of variation for January 1, 2014, 558nm (green). The red line is found per Eq 3.12 from Y, and the black line from the pre-flat field keogram C.

relative noise to be considered, due to dimmer light and a less sensitive spectrograph sensor.

$$\begin{cases} \text{if } c_{v,558nm} > 0.25, \text{ cloud free} \\ \text{if } c_{v,630nm} > 0.4, \text{ cloud free} \\ \text{otherwise, cloudy} \end{cases} \tag{3.13}$$

A high c_v metric in either 558 nm (green) or 630 nm (red) designates cloud-free instants. A minimum of two consecutive cloud free timesteps, corresponding to the keogram snapshots every 14 s, is designated a cloud-free interval, which is used for the spectral analysis in Chapter 4.

As a final remark c_v is expected to be sensitive to noise during dim light. In a hypothetical totally dark sky, noise is still present, and is captured in the standard deviation of the keogram snapshot ($\sigma = \sigma_\nu$), but mean intensity is low ($\mu \approx 0$), so the coefficient of variation appears artificially large, and regardless of actual cloud cover is designated cloud-free. However, this was not observed in nights used to decide the c_v threshold. To preclude this possibility, a check for very low mean intensity ($\mu \approx 0$) could be added.

CHAPTER 4

SPECTRAL CLASSIFICATION OF IONOSPHERE LAYER

With clear all-sky images (ASIs) of aurora, the characteristic energy of driving electron precipitation and thus the altitude of the irregularity layer is determined. Cloud-free intervals (determined by keogram as described in Chapter 3), the ASI database [15], and the SAGA scintillation event list [12] are combined to identify events with the prerequisite conditions for analysis: the occurrence of scintillation, the availability of all-sky images, and the determination that they have cloud-free conditions. In this chapter, I discuss how ASIs are calibrated for wavelength sensitivity and bias. Scintillating satellites far from magnetic zenith are removed from consideration, and the satellite pixels of remaining times identified. They are categorized to be E- or F-layer, based on the red/blue intensity ratio using auroral theory. Figure 4.1 summarizes the processing that will be described in this chapter. The multiyear results will be presented and compared to radar classifications at the end of the chapter.

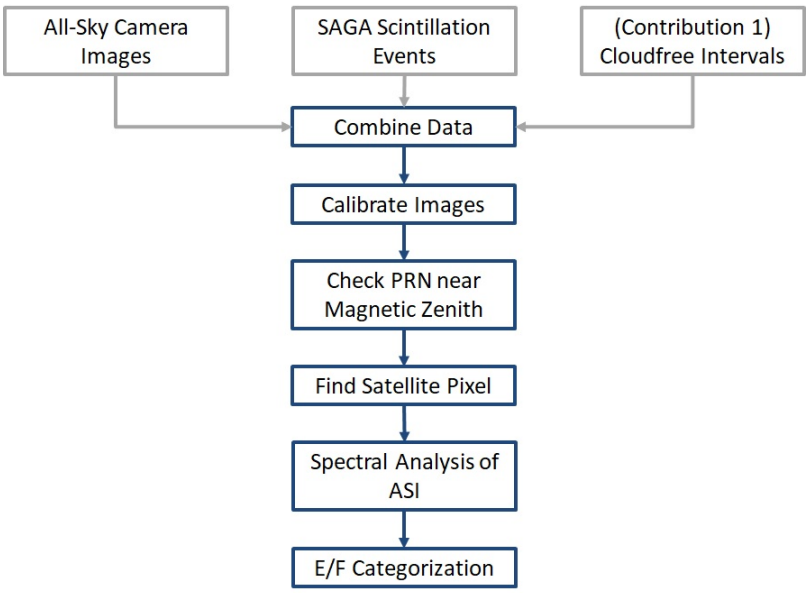

Figure 4.1. Overview of all-sky image processing.

4.1 ASI Data and Synthesis with SAGA and Keograms

Camera ASIs must be combined with the SAGA scintillation list and the cloud-free intervals from the keogram method. There are 3 necessary conditions before any image processing is done:

1. That a triplet of camera images be present at the instant.
2. That SAGA has identified an overlapping scintillation event.
3. That keogram cloud detection shows an overlapping cloud free interval.

ASIs are taken at the same wavelengths as the keograms, and stored as flexible image transport system (FITS) files on a server at [15]. Using MATLAB as an FTP client, directories for both years were downloaded, and a file list of all 2014-2015 images was created, along with a list of timestamps (timestamps are included in the file names). By comparing these times with the Scintillation Event List [7], a list of ASIs during scintillation is created. Again, with the same motivation to limit file transfer as the keogram method, only this 161 GB subset is downloaded. By referring to the cloud-free intervals identified with the keogram method (Chapter 3), a list of cloud-free ASIs during scintillation is created. This process is shown in Fig. 4.2.

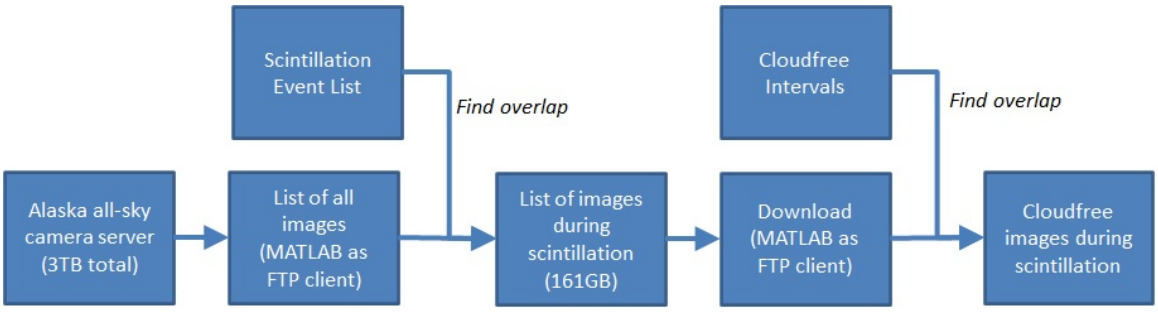

Figure 4.2. Steps for identifying ASIs during scintillation, their download, and identification of cloud-free images.

ASI FITS files include metadata, a part of which is shown in Fig 4.3 for the January 1, 2014, 11:00:05.592 UTC, 428 nm (blue) image. Exposure times are included, as are other camera settings.

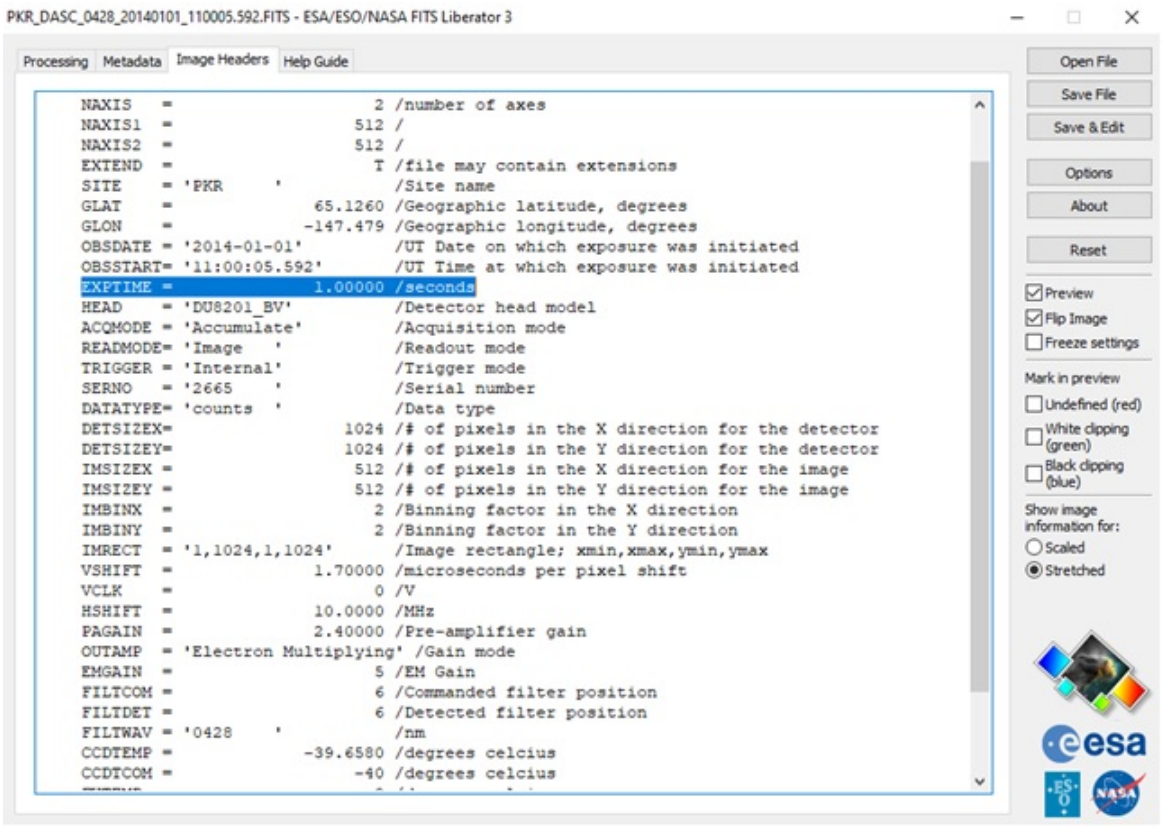

Figure 4.3. ASI FITS file header data viewed in FITS Liberator 3, showing timestamps, exposure time, and wavelength, and camera configurations.

4.2 ASI Calibration and Satellite Pixel Identification

ASI data is calibrated for exposure time, wavelength-specific sensor response, and bias. From raw images the bias is subtracted, then converted to physical units with known camera properties and exposure time. Equation 4.1 shows this calibration, where S is the raw sensor image (units of camera counts), β_λ is the constant bias (also in camera counts), k_λ is the wavelength-specific camera response per exposure time provided by [20], and e_λ is wavelength-specific exposure time (found in FITS file headers).

$$M_{\lambda,ij}(t) = [S_{\lambda,ij}(t)[\text{counts}] - \beta_\lambda] \left(\frac{k_\lambda}{e_\lambda}\right) \tag{4.1}$$

resulting in M the photon flux in Rayleighs.

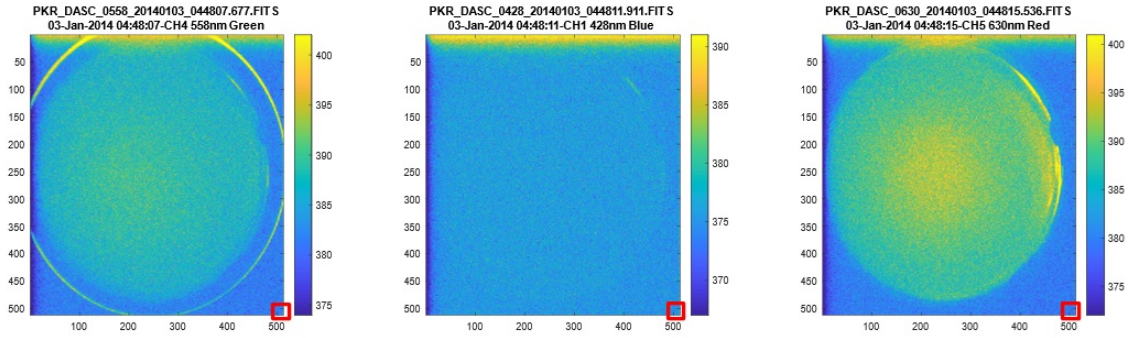

Figure 4.4. ASI triplet looking of images of dark sky on January 3, 2014, 04:48:07-04:48:15 UTC, used to find camera bias β. Scale shows camera units [counts], and corners outlined in a red box are the 12-by-12 pixel region averaged to estimate β. (left) 558 nm; (center) 428 nm; (right) 630 nm.

ASI calibration values, including calculated biases, are shown in Table 4.1. Biases are very similar, which is to be expected since the same sensor is used for all wavelengths. Similar to the keogram spectrograph, the camera is least sensitive to blue (428 nm) light, contributing to noisiness in that channel.

As a case study calibrated images of March 18, 2015, 08:06:13-08:06:21 UTC are presented in Fig. 4.5. These occur during the St. Patrick's Day 2015 geomagnetic storm, a well-studied event including by [8]. Auroral intensity is on the order of 10's

Table 4.1. ASI Calibration Values

Wavelength (λ)	ASC Calibration (k_λ)	Exposure Time (e_λ)	Bias (β_λ)
427.8nm	105 Rayleigh·s/Count	1.0 s	375 Counts
557.7nm	70 Rayleigh·s/Count	1.0 s	381 Counts
630.0nm	27 Rayleigh·s/Count	1.5 s	379 Counts

of kRayleighs, such that sensor noise is not immediately observable, in contrast to the per-pixel effects and sensor edge structures seen on the dark images in Fig 4.4.

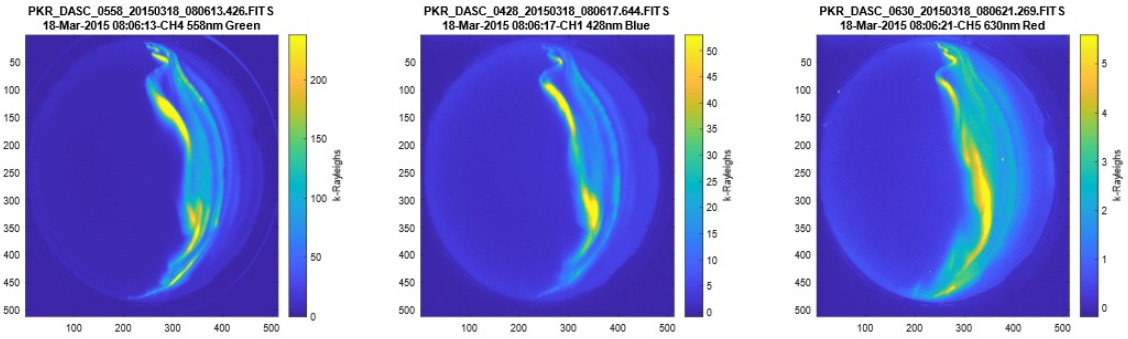

Figure 4.5. St. Patrick's Day 2015 Storm ASI calibrated triplet M on March 18, 2015, 08:06:13-08:06:21 UTC, showing distinct auroral arcs. (left) 558 nm; (center) 428 nm; (right) 630 nm.

SAGA measured detrended, filtered power and phase [5] for GPS satellite (PRN) 25 for the case study shown in Fig. 4.6. Phase scintillation, the prevalent mode in the auroral zone, is recorded.

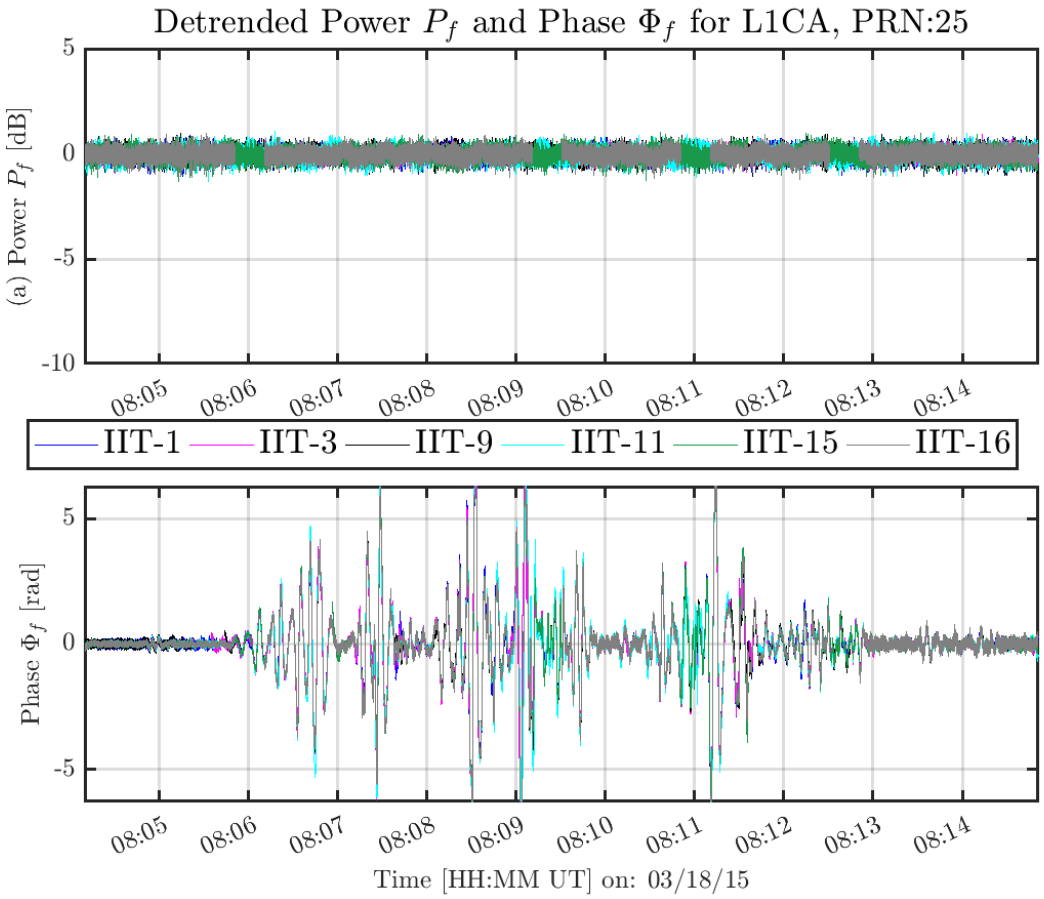

Figure 4.6. SAGA detrended, filtered 100 Hz GPS L1 frequency signal (a) power and (b) phase for PRN 25, March 3, 2015, 08:04-08:15 UTC from [12]. Significant phase scintillation is seen.

The column-integrated auroral analysis used to categorize ionosphere layer [2] requires viewing near magnetic zenith. Sounding rocket experiments established the limit as up to δ=25° away [20]. Magnetic zenith direction (azimuth/elevation) is known for Poker Flat. GPS satellite sky position is found by first referring to PRN number in the SAGA event list, and then to daily GPS Yuma almanacs [22], in order to compute the PRN's azimuth and elevation as viewed from Poker Flat. The $\delta < 25°$ threshold is applied, and ASI timestamps out of this bound are removed. This is represented in Fig 4.7. For the interval of a scintillation event, all contained ASI timestamps are treated this way. Events with all timestamps removed are discarded; the scattering layer will not be categorized. Partial or full portions of scintillation intervals, defined in this way, move forward in the analysis.

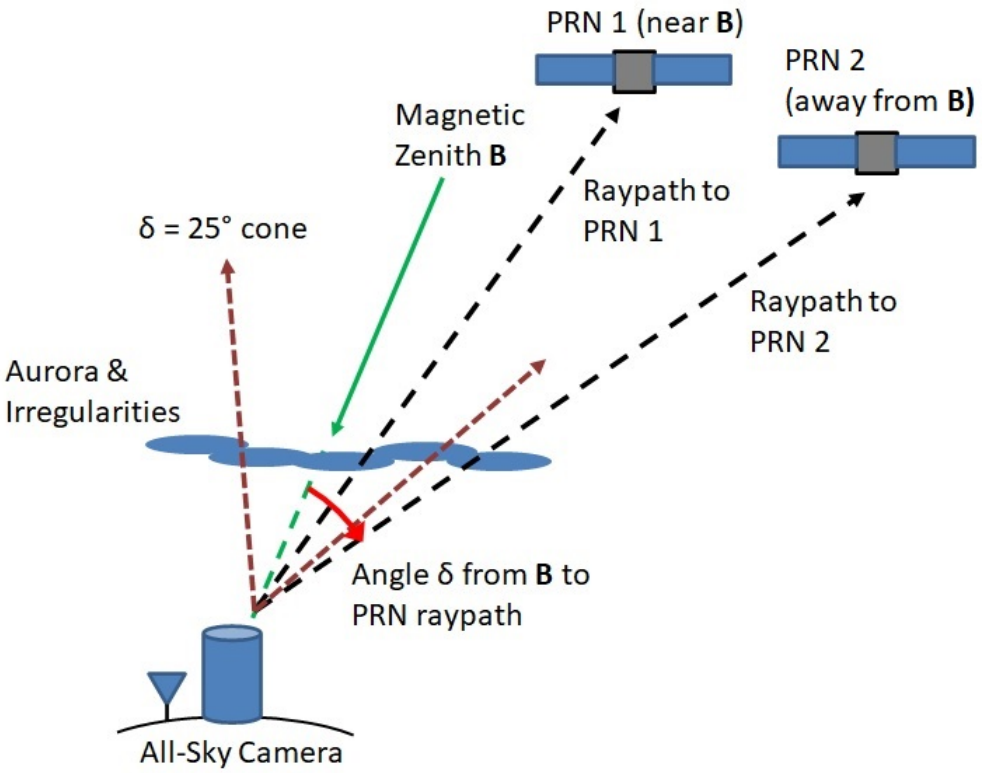

Figure 4.7. Threshold for scintillating PRNs near or far from magnetic zenith **B**. PRN 1 is within the cutoff, while PRN 2 is outside, so the scintillation for PRN 2 is not categorized with spectral analysis.

The satellite pixel locations in ASIs are found after some precalculation for efficiency. Mappings for each ASI pixel's look-direction in the sky are contained in two reference FITS files [15]. In cylindrical azimuth (degrees East-from-North) and elevation coordinates, mappings for pixels higher than 10° from the horizon are given. The pixel region within the $\delta < 25°$ threshold is found by finding the angle between each pixel and magnetic zenith. The cylindrical azimuth/elevation per-pixel mapping and magnetic zenith, are converted to arbitrary Cartesian coordinates (via the MATLAB sph2cart function), and dot products calculated to find angle between the two. Pixels with $\delta > 25°$ are discarded from further analysis. Surviving pixels are in the oval region of Fig. 4.8, where magnetic zenith is the red 'x'. This process is performed only once for algorithmic efficiency.

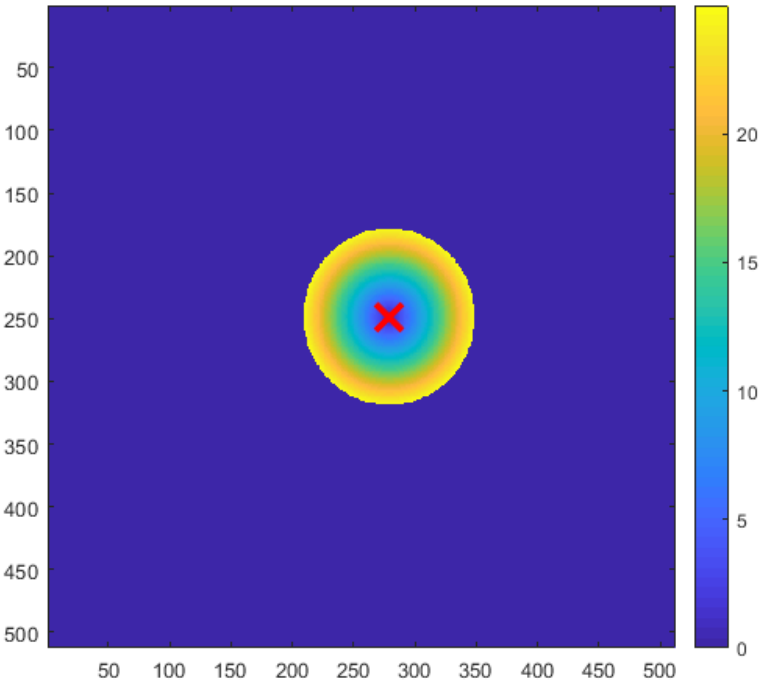

Figure 4.8. Pixel regions of interest in all-sky images. Color scale represents angle between each pixel and magnetic zenith 'x,' from $\delta = 0°$ (dark blue) to 25° degrees (yellow). Not mapped outside oval region.

At ASI scintillation timestamps, the angle between all pixels in the precalculated region and satellite raypath is calculated in the same manner as determining angle to magnetic zenith. The pixel (i^*, j^*) corresponding to the minimum is identified as the satellite pixel. Since only pixels near magnetic zenith are considered instead of the entire image, algorithm complexity is reduced.

4.3 E/F Event Categorization

As described in the Introduction, auroral theory provides the relation between observed constituent emissions and electron characteristic energy, α [2], which is used to estimate auroral height [11]. Aurorae at 100-150 km are driven by precipitation with α of 2-10 keV [11], so 2 keV is used as the threshold for the E/F transition (more energetic precipitation penetrates deeper in the ionosphere). The model provided by Rees and Luckey [2] provides best sensitivity for α by using the red/blue (630 nm/428 nm) ratio ρ, along with blue emission intensity M_{428,i^*j^*}. This model has α=2 keV with a nearly constant red/blue ratio of 0.5, independent of blue intensity. Only a broad E- or F-layer classification is sought, not a more granular height, so irregularity layers are thus categorized by:

$$\begin{aligned} &\text{if } \rho_{630/428} <= 0.5, \text{ E-region irregularity instant} \\ &\text{if } \rho_{630/428} > 0.5, \text{ F-region irregularity instant} \end{aligned} \tag{4.2}$$

ASI image triplets are taken in the order red-green-blue, at a cadence of 12.5s as shown below in Fig 4.9. To facilitate analysis of α found from any of the three combination of emissions, a working list of triplets is ordered as green-blue-red. This gives minimum delay between a triplets blue and red image, which are now subsequent, unlike the original ordering. While the emission model [2] assumes a steady-state column, aurorae are dynamic, so imaging delays should be minimized.

The three ratios (red/blue, green/blue, red/green) are presented in Fig 4.10

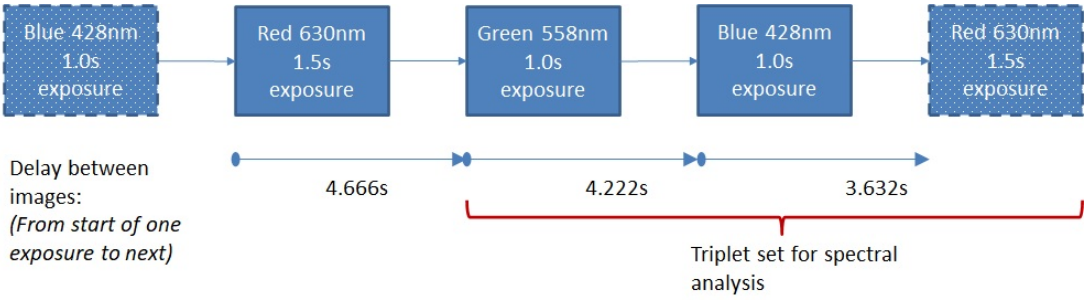

Figure 4.9. Order camera images are taken, with exposure times and delays between exposure starts. A green/blue/red order is selected as for analysis.

for the St. Patrick's Day Storm case study March 18, 2015, 08:06:13 UTC. While intensities showed similar profiles (Fig 4.5), ratios show greater difference and unique structures. Auroral arc motion and magnetic zenith orientation [8], coupled with longer half-life of red-emitting oxygen species, may create apparent ratios on arc edges that aren't representative of instantaneous electron precipitation α. A hypothetical fast-moving arc with uniform α would leave longer-lasting atomic oxygen with persistent red emissions. However shorter-lived nitrogen ions quickly decay, so the blue emissions reflect a shorter timescale. As a result, the trailing edge of the arc may appear redder in terms of ratio, and have a bias towards F-Layer classification. At this instant the bulk auroral arc has just started moving northward (i.e., toward the left of each image), though feature movement is not uniform.

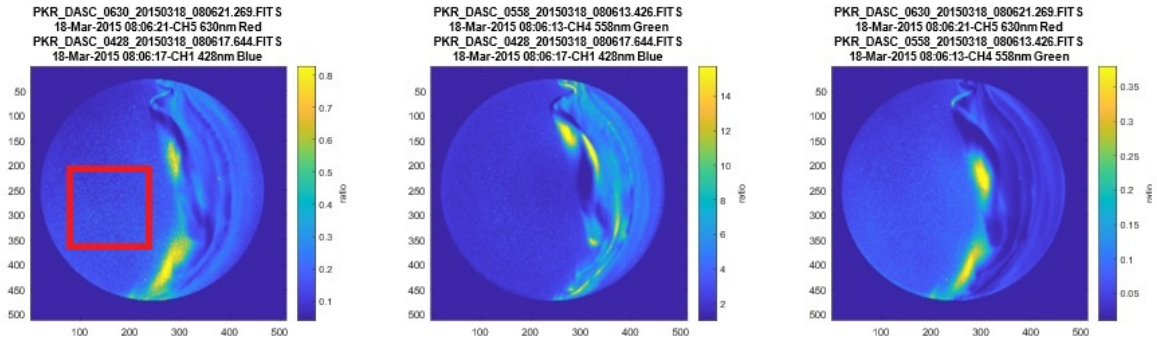

Figure 4.10. Ratios of wavelength emissions measured by the ASI, calculated at each pixel. Dim region with high per-pixel noise highlighted with the red box. (left) red/blue; (center) green/blue; (right) red/green ratio.

Fig 4.10 also shows greater per-pixel variation (presumably noise) in the dim regions absent auroral arcs, highlighted in the red box. In these regions the signal-to-noise ratio is higher, and is exacerbated by placing a small column emission value in the denominator (of the ratio). Though scintillation events in areas of the sky absent aurora have not been observed within the ASIs manually reviewed, if present another technique would be needed for these times' layer categorizations.

Layer categorization of entire scintillation intervals is made from categorizations at each ASI timestamp. Categorizations are first assigned every 12.5s for triplet sets during scintillation intervals using the intensities at pixel (i^*, j^*), then the majority of those during the scintillation time interval is found. In the event of a tie, E-layer is assigned, as the 150 km cutoff is a lower definition of the E-layer used by a separate radar method [7] used for comparison later in the chapter.

For the St. Patrick's Day storm case study, the red/blue ratio image is enlarged in Fig. 4.11, with magnetic zenith marked by the green circle, and the 3 simultaneously scintillating PRNs 25, 29, and 31 identified by the automated scintillation detection and classification method [7] marked by the magenta '+', magenta triangle, and red 'x,' respectively. PRN 31 lies too far from magnetic zenith for categorization. PRN 25 has a ratio of $\rho_{630/428} = 0.13$, and PRN 29 a ratio of $\rho_{630/428} = 0.28$, so both are designated E-region at this instant. The red arrow highlights a region near magnetic zenith of relatively stronger red light, where, had a PRN been present at that point, it would have been categorized as F-layer. This shows the layer categorization is not necessarily uniform for all parts of the sky at the same instant.

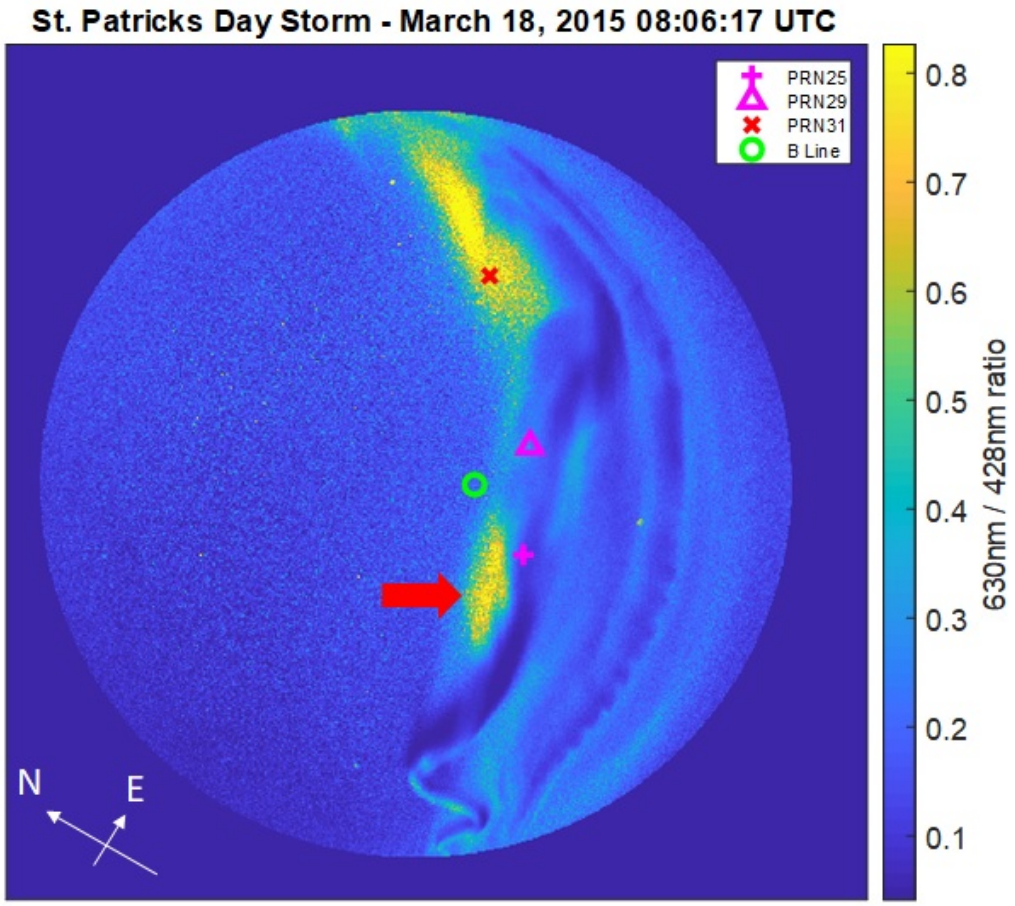

Figure 4.11. Red/blue ratio for St. Patrick's Day (March 18, 2015 08:06 UTC) case study. Magnetic zenith is marked by the green circle. PRN 25 and 29 are marked by the magenta cross and triangle, respectively. PRN 31 is the red 'x'. Red arrow highlights region of relatively stronger red light.

Poker Flat incoherent scatter radar electron density measurements (color) as a function of time and altitude on March 18, 2015, are shown in Fig 4.12. The solid vertical lines mark the scintillation time interval of PRNs 25 and 29 as detected by SAGA. The dashed vertical lines mark the scintillation event detected for PRN 31. The horizontal line at 195 km divides the altitudes sensed by two different radar pulse types: above 195 km the long pulse is used and below 195 km the alternating code measurements are used [7]. The scattering layer is assigned by the altitude of peak electron density, with 150km (lower black line) the threshold between the lower E- and higher F-layer. Though the PFISR beam points at magnetic zenith rather than tracking the satellite, the radar measures electron density maxima in the E-region as well.

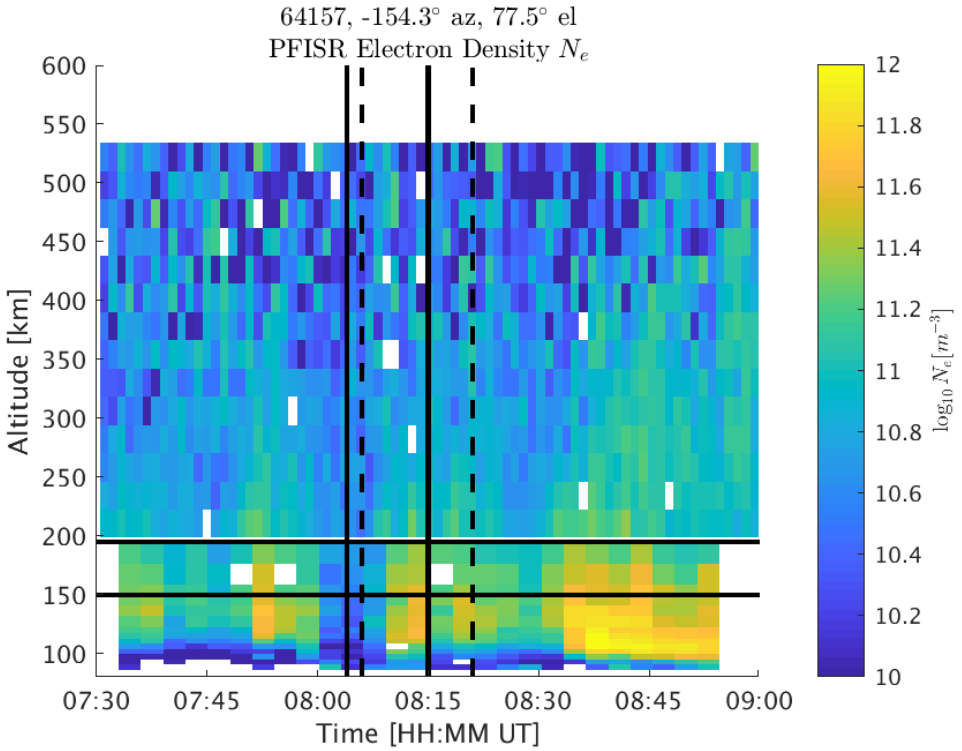

Figure 4.12. PFISR electron density measurements in magnetic zenith direction, March, 18 2015 7:30-9:00 UTC, plotted following the method of [7]. Peak density for 08:06 UTC is seen in the E-region.

4.4 Multiyear Results and Comparison with Radar

Categorizations assigned for 2014-2015 scintillation events are shown in Table 4.2. These are the assignments based on the simple majority of ASIs within scintillation intervals, and not total numbers of images. A total of 4174 phase scinitillations at L1 or L2C were detected by SAGA for the two years [7]. None of the few amplitude or amplitude-and-phase scintillation events met all conditions for ASI categorization. In the table the phase scintillation events are broken into year and L1/L2C frequency by row. Moving left-to-right from the SAGA Events column, events detected as cloud free are shown, with the corresponding percentage of original SAGA events. For example, for 2014 L1 events, 418 are cloud free, which is 42.0% of all SAGA detected scintillations for that category. The next column shows the total number of cloud-free events meeting conditions for ASI analysis (i.e., ASI files present and a healthy PRN near magnetic zenith), and the percentage of cloud free events that are near magnetic zenith. The rightmost E-Layer and F-Layer columns show final ASI layer categorizations, and percentages of layer-categorized events, of the events occurring near magnetic zenith.

The keogram cloud detection detected more cloudy times in 2015 than 2014, where only 1/6 of and 1/2 of events respectively were found cloud free. For all scintillation categories a consistent 30% of events had the PRN near magnetic zenith. Layer designations are made only for the 364 events in the final columns. A majority (77.5%) of all categorized events are F-layer, and a minority (22.5%) E-layer.

Table 4.2. ASI Spectral Analysis Multiyear Irregularity Layer Categorizations

Scintillation Category	SAGA Events	Of Those Cloud Free	Of Those Near Magnetic Zenith	E-Layer	F-Layer
2014 L1	996	418	143	36	107
		42.0%	34.2%	25.2%	74.8%
2015 L1	1677	305	99	23	76
		18.2%	32.5%	23.2%	76.8%
2014 L2	553	238	65	13	52
		43.0%	27.3%	20.0%	80.0%
2015 L2	185	418	57	10	47
		19.5%	30.8%	17.5%	82.5%
Total	4174	1146	364	82	282
		27.5%	31.8%	22.5%	77.5%

The 364 events with categorizations estimated by ASI are compared with their PFISR electron density categorizations [7] in Table 4.3. Ignoring the 184 events missing radar data, a majority (60.5%) of radar classifications are E-Layer, and a minority (28.3%) F-Layer. By comparing only the subset of events with ASI categorization, some structural difference in the 2 methods are avoided - ASI is inoperable mid-spring through autumn due to longer days, and during day. However, there is likely some selection bias in the missing radar data, as PFISR operates selectively when other radar experiments are also active [14].

The discrepancy presents the question whether underlying physics or different experimental methods create the difference. ASI fundamentally measures active ionization, while radar measures electron density, and scintillation is driven by around 100 m scale irregularities in electron density gradients. By being fixed at magnetic zenith PFISR analysis presents a limitation demonstrated with the St. Patrick's Storm case study, where the active ionosphere layer is not constant for the entire sky at the same time (assuming the spectral analysis is correct). The spectral analysis

Table 4.3. ASI Categorized Events Compared to PFISR Results

Scintillation Category	ASI E-Layer	ASI F-Layer	PFISR E-Layer	PFISR F-Layer	PFISR Ambiguous	PFISR Missing Data
2014 L1	36	107	60	30	12	41
	25.2%	74.8%	42.0%	21.0%	8.4%	28.7%
2015 L1	23	76	16	1	2	80
	23.2%	76.8%	16.2%	1.0%	2.0%	80.8%
2014 L2	13	52	25	19	6	15
	20.0%	80.0%	38.5%	29.2%	9.2%	23.1%
2015 L2	10	47	8	1	0	48
	17.5%	82.5%	14.0%	1.8%	0.0%	84.2%
Total	82	282	109	51	20	184
	22.5%	77.5%	29.9%	14.0%	5.5%	50.5%

may be improved by applying more nuanced auroral models incorporating neutral behavior, such as the GLOW model [23]. The differences in E- vs. F-layer dynamics motivates the need for obtaining the categorization in the first place, as neutral flows influence plasma velocity in the E-region, but not the F-region where they are more sparse. As red emissions predominately occur at the F-layer unaffected by neutrals, but blue emissions occur in the E-layer with more concentrated neutrals, there will be some difference in field-perpendicular plasma velocity with height. The ASI column-integrated aurora methods do not account for field-perpendicular transport, so may be less suited for E-layer events, though this does not explain the discrepancy.

CHAPTER 5
CONCLUSION

5.1 Summary

The first contribution of this work is an automated keogram cloud detection method combining a flat field correction step with coefficient of variation to determine cloudiness from keogram snapshots. Leveraging the compact data sizes of keograms compared to full ASIs, the method was found capable of flagging cloudy times. Times with residual sunlight, as well as regions near the horizon were removed, and the background keogram subtracted to remove light pollution. With a manually identified interval of total cloud cover, an average cloudy flat field was constructed, and thus an average flat field gain. This gain was applied to a full two-year set of keogram data to normalize for cloudy behavior as well as remove lens and sensor artifacts. The coefficient of variation c_v is found for each corrected snapshot as the cloud detection metric. Thresholds of 0.25 for 558 nm (green) and 0.4 for 630 nm (red) are used to determine cloudiness, while 428 nm (blue) exhibits excess noise for consideration. A high c_v metric in either 558 nm (green) or 630 nm (red) designates cloud-free instants. Flat fielding improves c_v sensitivity to cloudiness, as the pre-flat field c_v for cloudy snapshots shows a higher floor. This method offers physically-based an alternative to prior research using machine learning techniques.

The second contribution of this work is applying spectral analysis to full ASIs during scintillation to determine the ionosphere layer of irregularities. Successive requirements are checked, with layer categorizations given to those meeting all conditions. First, three data sets are combined: cloud free intervals (from the first contribution), the SAGA scintillation event list, and the directory of 2014-2015 ASIs, to create a preliminary list of times for analysis. A subset of ASI files is transferred to a local machine. ASIs are calibrated with known camera parameters, and camera

biases identified from dark sky images and removed.

A scintillating PRN's position in the sky at Poker Flat is found with daily YUMA GPS almanacs, also removing PRNs for which no almanac data are available (presumed unhealthy PRNs). The spectral analysis relies on a scintillation ray path aligned with an auroral column (i.e., aligned with magnetic zenith) to within 25°. Electrons precipitate along magnetic field lines, so the angle δ between magnetic zenith and PRN is found, and events too far from magnetic zenith are discarded. With a supplied azimuth/elevation pixel mapping for look direction, a subset of pixels meeting the requirement of $\delta < 25°$ is created, and the pixel nearest to the PRN direction identified.

At the satellite pixel the active ionosphere layer is found. Combining observations of auroral heights as a function of electron characteristic energy α [11], with an auroral chemistry model [2], a red/blue ratio threshold of 0.5 separates lower ratios as E-region and higher ratios F-Region events. Categorizations are made for each scintillating triplet, and the majority of triplet designations during scintillation intervals categorizing the overall event. A case study for the March 18, 2015, St. Patrick's Day storm demonstrates the method with multiple simultaneous scintillations present, and shows different directions in the same sky time can return different classifications.

Ionosphere layer categorizations for the 364 events in 2014-2015 meeting requisite conditions are presented, 77% of them F-region and 23% E-region. Cloud detection removed half of 2014 events but 5/6 of 2015 events, and PRN nearness to magnetic zenith removed a consistent 2/3 events across categories. Similar results were seen for L1 and L2C events. Turning to the radar scattering layer categorizations by PFISR [7], of the 364 events an estimate was made for 180 of those, of which the majority are E-Region. Disagreement between the methods is possibly explained by selection bias in PFISR operation, differences in E- and F-Layer velocity dynamics

due to neutral flow, ASI measuring active ionization as opposed to radar's electron density, or rapid auroral arc motion not represented by steady-state auroral chemistry models.

5.2 Future Work

Refinements exist for the keogram cloud detection method. A more accurate cloudy flat field may be constructed from multiple nights across both years, rather than a single night. Coefficient of variation thresholds may be improved and better characterized by establishing the error matrix of true positives, true negatives, false positives, and false negatives for this detector, by comparing the predicted cloudiness with the true state using a large set of manually reviewed ASIs. The limitation is the need to manually review hundreds of ASIs to form a truth reference. Moonlight is currently uncorrected for as a source of non-auroral light which skews both cloud detection and ASI analysis if present, and can be flagged. Also cloudiness of the sky gradually changes, and adjacent times of cloudiness will have some correlation, future work can incorporate a hidden markov model to improve the accuracy of the detector.

The layer categorization disagreement between ASI and PFISR is an open question. Neutral flows influencing plasma dynamics in the E-layer may play a role. For ASI analysis both spatial and temporal averaging of emissions around PRN scintillations can be applied to minimize noisiness and artifacts from auroral motion. ASI biases can be modelled with dark images throughout the year, rather than a single night, to account for sensor drift over the years. An updated auroral chemistry model incorporating more nuanced neutral conditions, such as the GLOW model [23], can replace the Rees and Luckey model. As PFISR results currently disagree significantly with my ASI method, sensitivity analysis of varying the 630nm/428nm ratio threshold for E/F categorization, and tighter limits on PRN nearness to magnetic zenith, may be informative. Concerning scintillation measurement, occasional gaps in scin-

tillation measurements during heavy solar activity may be addressed with emerging signal acquisition techniques, such as [24]. Finally as the instrumentation has run continuously since late 2013, this method can be extended through 2019 and beyond, capturing an entire half-solar cycle.

BIBLIOGRAPHY

[1] T. F. Tascione, *Introduction to the Space Environment*, 2nd ed. Malabar, Florida: Krieger Publishing Company, 1994.

[2] M. H. Rees and D. Luckey, "Auroral electron energy derived from ratio of spectroscopic emissions 1. model computations," *Journal of Geophysical Research*, vol. 79, no. 34, pp. 5181–5186, January 1974.

[3] D. Anderson and T. Fuller-Rowell. (1999) Various layers of the ionosphere and their predominant ion populations are listed at their respective heights above ground. The density in the ionosphere varies considerably, as shown. [Online]. Available: NOAA: http://www.sel.noaa.gov/info/Iono.pdf.

[4] K. C. Yeh and C. H. Liu, "Radio wave scintillations in the ionosphere," *Proceedings of the IEEE*, vol. 70, no. 4, pp. 324–360, April 1982.

[5] Y. Su, S. Datta-Barua, G. S. Bust, and K. B. Deshpande, "Distributed sensing of ionospheric irregularities with a gnss receiver array," *Radio Science*, vol. 52, no. 8, pp. 988–1003, June 2017.

[6] R. Parvizi, H. S. Zadeh, L. Pan, B. Pervan, and S. Datta-Barua, "Multi-sensor study of lake michigan's surface using gnss-reflectometry," in *Proceedings of the 31st International Technical Meeting of The Satellite Division of the Institute of Navigation (ION GNSS+ 2018)*, 2018.

[7] V. Sreenivash, Y. Su, and S. Datta-Barua, "Automated ionospheric scattering layer hypothesis generation for detected and classified auroral global positioning system scintillation events," *Radio Science*, vol. 55, no. 1, January 2020.

[8] S. Mrak, J. Semeter, M. Hirsch, G. S. D. Hampton, R. H. Varney, A. S. Reimer, J. Swoboda, P. J. Erickson, F. Lind, A. J. Coster, and V. Pankratius, "Field-aligned gps scintillation: Multisensor data fusion," *Journal of Geophysical Research: Space Physics*, vol. 123, no. 1, pp. 974–992, January 2018.

[9] "Solar wind interaction," Norwegian Centre for Space Weather, 11-Apr-2020. [Online]. Available: https://site.uit.no/spaceweather/what-are-the-northern-lights-aurora/. [Accessed: 20-Apr-2020].

[10] D. J. Strickland, R. R. Meier, J. H. Hecht, and A. B. Christensen, "Deducing composition and incident electron spectra from ground-based auroral optical measurements: Theory and model results," *Journal of Geophysical Research*, vol. 94, no. A10, pp. 13 527–13 539, October 1989.

[11] P. M. Banks, C. R. Chappell, and A. F. Nagy, "A new model for the interaction of auroral electrons with the atmosphere: Spectral degradation, backscatter, optical emission, and ionization," *Journal of Geophysical Research*, vol. 79, no. 10, pp. 1459–1470, April 1974.

[12] "Welcome to Our Data Archive!," Space Weather Lab at IIT. [Online]. Available: http://apollo.tbc.iit.edu/ spaceweather/live/?q=SAGA. [Accessed: 15-Mar-2020].

[13] R. Parvizi, B. Pervan, and S. Datta-Barua, "Surface ice reflectometry with a dedicated gnss receiver i: Hardware and field test," N.D., under review.

[14] "Welcome to the NEW Madrigal Database at SRI International," Madrigal Database. [Online]. Available: http://isr.sri.com/madrigal/. [Accessed: 19-Jan-2020].

[15] D. Hampton, "Archive Data," Optics. [Online]. Available: http://optics.gi.alaska.edu/optics/archive. [Accessed: 19-Apr-2020].

[16] D. Olsen, C. Dou, X. Zhang, L. Hu, H. Kim, and E. Hildum, "Radiometric calibration for agcam," *Remote Sensing*, vol. 2, pp. 464–477, February 2010.

[17] J. A. Seibert, J. M. Boone, and K. K. Lindforsand, "Flat-field correction technique for digital detectors," *Medical Imaging 1998: Physics of Medical Imaging*, July 1998.

[18] L. Clausen and H. Nickisch, "Automatic classification of auroral images from the oslo auroral themis (oath) data set using machine learning," *J. Geophys. Res.*, vol. 123, July 2018.

[19] J. Rao, N. Partamies, O. Amariutei, M. Syrjasuo, and K. E. A. V. D. Sande, "Automatic classification of auroral images from the oslo auroral themis (oath) data set using machine learning," *J. Geophys. Res.*, vol. 123, July 2018.

[20] D. Hampton, private communication. February 2019.

[21] "Barcode," Wikipedia, 11-Apr-2020. [Online]. Available: https://en.wikipedia.org/wiki/Barcode. [Accessed: 19-Apr-2020].

[22] "GPS ALMANACS, NANUS, AND OPS ADVISORIES ARCHIVES," U.S. Coast Guard Navigation Center. [Online]. Available: https://www.navcen.uscg.gov/?Do=gpsArchives. [Accessed: 18-Apr-2020].

[23] S. C. Solomon, "Global modeling of thermospheric airglow in the far ultraviolet," *Journal of Geophysical Research: Space Physics*, vol. 122, no. 7, pp. 7834–7848, July 2017.

[24] R. Parvizi and S. Datta-Barua, "Surface ice reflectometry with a dedicated gnss receiver ii: Signal processing enabling acquisition from reflected signals," N.D., under review.